

Assembly Principles of the Human R2TP Chaperone Complex Reveal the Presence of R2T and R2P Complexes

Thiago V. Seraphim^{1,2,11}, Nardin Nano^{1,11}, Yiu Wing Sunny Cheung¹, Siripat Aluksanasuwan^{1,3,a}, Carolina Colleti^{1,4}, Yu-Qian Mao¹, Vaibhav Bhandari¹, Gavin Young⁵, Larissa Höll², Sadhna Phanse^{1,2}, Yuliya Gordiyenko⁵, Daniel R. Southworth⁶, Carol V. Robinson⁵, Visith Thongboonkerd³, Lisandra M. Gava⁴, Júlio C. Borges⁷, Mohan Babu², Leandro R. S. Barbosa⁸, Carlos H. I. Ramos⁹, Philipp Kukura⁵, Walid A. Houry^{1,10,12,*}

¹Department of Biochemistry, University of Toronto, Toronto, ON M5G 1M1, Canada

²Department of Chemistry and Biochemistry, University of Regina, Regina, SK S4S 0A2, Canada.

³Medical Proteomics Unit, Office for Research and Development, Faculty of Medicine Siriraj Hospital, Mahidol University, Bangkok, Thailand.

⁴Center of Biological and Health Sciences, Federal University of São Carlos, São Carlos, SP 13560-970, Brazil.

⁵Physical and Theoretical Chemistry Laboratory, Department of Chemistry, University of Oxford, Oxford OX1 3QZ, UK.

⁶Department of Biochemistry and Biophysics, Institute for Neurodegenerative Diseases, University of California, San Francisco, CA 94158, USA.

⁷São Carlos Institute of Chemistry, University of São Paulo, São Carlos, SP 13566-590, Brazil.

⁸Institute of Physics, University of São Paulo, São Paulo SP, 05508-090, Brazil; and Brazilian Synchrotron Light Laboratory, Brazilian Center for Research in Energy and Materials, Campinas SP, 13083-100, Brazil.

⁹Institute of Chemistry, University of Campinas UNICAMP, Campinas SP, 13083-970, Brazil.

¹⁰Department of Chemistry, University of Toronto, Toronto, Ontario M5S 3H6, Canada.

¹¹These authors contributed equally.

¹²Lead contact

^aCurrent address: School of Medicine, Mae Fah Luang University, Chiang Rai, Thailand.

*Correspondence: W. A. Houry, Department of Biochemistry, University of Toronto, 661 University Avenue, MaRS Centre, West Tower, Room 1612, Toronto, ON M5G 1M1, Canada.
Tel.: (416) 946-7141; Fax: (416) 978-8548; Email: walid.houry@utoronto.ca

SUMMARY

R2TP is a highly conserved chaperone complex formed by two AAA+ ATPases, RUVBL1 and RUVBL2, that associate with PIH1D1 and RPAP3 proteins. R2TP acts in promoting macromolecular complex formation. Here, we establish the principles of R2TP assembly. Three distinct RUVBL1/2-based complexes are identified: R2TP, RUVBL1/2-RPAP3 (R2T), and RUVBL1/2-PIH1D1 (R2P). Interestingly, we find that PIH1D1 does not bind to RUVBL1/RUVBL2 in R2TP and does not function as a nucleotide exchange factor; instead, RPAP3 is found to be the central subunit coordinating R2TP architecture and linking PIH1D1 and RUVBL1/2. We also report that RPAP3 contains an intrinsically disordered N-terminal domain mediating interactions with substrates whose sequences are primarily enriched for armadillo repeat domains and other helical-type domains. Our work provides a clear and consistent model of R2TP complex structure and gives important insights into how a chaperone machine concerned with assembly of folded proteins into multisubunit complexes might work.

(147 words)

Keywords: AAA+ proteins, molecular chaperones, R2TP, PAQosome, macromolecular complex, protein folding, ATPases

INTRODUCTION

The R2TP chaperone complex was initially discovered by our group in a systematic proteome-wide screen for Hsp90-interacting proteins in yeast (Zhao et al., 2005). The complex was then found to be conserved in all higher eukaryotes. In humans, R2TP consists of RUVBL1, RUVBL2, PIH1D1 and RPAP3 (Figure 1). R2TP was found to play critical roles in the assembly of macromolecular complexes regulating central cellular functions, such as cell response to nutrients, DNA damage response, ribosome biogenesis, RNA transcription and processing (Houry et al., 2018).

The R2TP complex has been shown to stabilize client proteins belonging to phosphatidylinositol 3-kinase-related kinases (PIKKs) family, such as mTOR, ATM, ATR, DNA-PKcs, and SMG-1, via interaction with the TTT complex (TELO2-TTI1-TTI2) (Cloutier et al., 2017; Horejsi et al., 2010; Kamano et al., 2013; Pal et al., 2021). R2TP is also involved in the assembly of the TSC complex (TSC1-TSC2-TBC1D7), a regulator of mTORC1, U5 snRNPs and L7Ae RNPs, (Cloutier *et al.*, 2017; Malinova et al., 2017; Mir et al., 2015) and RNA polymerase II (Boulon et al., 2010). More recently, R2TP and R2TP-like complexes have been associated to dynein assembly (Maurizy et al., 2018; Zur Lage et al., 2018). Biochemical and cell biological studies led to the hypothesis that R2TP functions as an assembly platform, bridging interactions between client proteins and chaperones, like HSP70 and HSP90, in order to promote quaternary structure formation (Martino et al., 2018; Rivera-Calzada et al., 2017).

RUVBL1 and RUVBL2 (Figure 1A) belong to the AAA+ superfamily (ATPases Associated with diverse cellular Activities) of P-loop NTPases, bearing Walker A and Walker B motifs required for nucleotide binding and hydrolysis (Seraphim and Houry, 2020). These motifs are encompassed within the $\alpha\beta\alpha$ domain I (DI), while the α -helical domain III (DIII) contains a *trans*-acting Arg (R-finger) (Seraphim and Houry, 2020). DI is divided into two subdomains by the so-called insertion or domain II (DII) (Figure 1A). DII was recently

proposed to be conformationally controlled via nucleotide binding (Matias et al., 2006; Silva et al., 2018a). DII contains an internal part (DII_{int}) located close to DI and DIII and an external OB-fold region (DII_{ext}) protruding from the RUVBL protomer. Typically, RUVBL1 and RUVBL2 assemble into heterohexameric complexes that can also associate via DII_{ext} to form double-heterohexameric species (Lakomek et al., 2015; Lopez-Perrote et al., 2012).

PIH1D1 has a PIH1 domain (Figure 1A) at the N-terminus that binds to peptides containing phosphorylated DSDD/E motifs present in TELO2 and MRE11 (Horejsi et al., 2014; von Morgen et al., 2017). PIH1D1 also contains a C-terminal CS domain (CHORD-containing proteins and SGT1) that binds to RPAP3 (Henri et al., 2018a). RPAP3 is the largest R2TP subunit, bearing an uncharacterized N-terminal domain (ND), two TPR domains (TPR1 and TPR2) that bind to the C-terminal EEVD motif of HSP90, and an intrinsically disordered region (IDR) connecting the TPR2 to the C-terminal domain (CD) (Figure 1A) (Henri *et al.*, 2018a; Maurizy *et al.*, 2018). Moreover, RPAP3 has been shown to have two isoforms in the cell (RPAP3 iso1 and iso2; Figure 1A), but only isoform 1 interacts with PIH1D1 (Yoshida et al., 2013).

Recently, cryo-electron microscopy studies revealed that, in human R2TP, RUVBL2 DIII binds RPAP3 CD, while DII binds to PIH1D1 (Martino *et al.*, 2018). Furthermore, PIH1D1 has been proposed to function as a nucleotide exchange factor (NEF) for R2TP, inducing conformational changes that result in the opening of the heterohexameric ring, hence, modulating the accessibility of the ATP-binding pocket of RUVBL1/2 (Munoz-Hernandez et al., 2019).

Here, we report a detailed biophysical and biochemical analysis of the human R2TP subunits and their binding interfaces. By using size exclusion chromatography coupled to static light scattering (SEC-MALS), small angle X-ray scattering (SAXS), and mass photometry, we report low-resolution solution structures of the RUVBL1/2 heterohexamer, RPAP3, and

RPAP3-PIH1D1, as well as their stoichiometry. Spectroscopic and mass spectrometry analyses revealed that RPAP3 ND is intrinsically disordered and mediates protein-protein interaction. Using pull-down experiments, we revealed that PIH1D1 does not bind directly to RUVBL1/2 in the R2TP complex. Our work shows that RPAP3 is the only link between RUVBL1/2 and PIH1D1 in R2TP and that RPAP3 contains two RUVBL-binding regions. RPAP3 and PIH1D1 were found to compete for RUVBL1/2 binding, hence, forming R2T (RUVBL1-RUVBL2-RPAP3) and R2P (RUVBL1-RUVBL2-PIH1D1) complexes, both *in vitro* and in cells. We also demonstrate, based on ATPase and nucleotide binding affinity assays, that PIH1D1 is not a NEF as reported (Munoz-Hernandez *et al.*, 2019). Our solution-based characterization allows us to propose detailed models for the assembly of human R2TP, R2T and R2P. These models highlight the critical role played by the DII domains of the RUVBLs in dictating the architecture of these complexes and clarifies several issues raised by the recent cryo-EM R2TP structures.

RESULTS

Solution structure of human RUVBL1 and RUVBL2

We purified recombinant untagged human RUVBL1 and RUVBL2 in their folded state (Figure S1) and initially evaluated their solution behavior by SEC-MALS (Figure 2A, Table S1). RUVBL1 alone behaved as a monomer at concentrations from 1 to 5 mg/mL (19.9 to 99.5 μ M protomer). However, at similar concentrations (19.5 to 97.7 μ M protomer), RUVBL2 formed monomers and hexamers. Analytical SEC (Figure S2A) and NanoESI experiments (Figure S2B) supported the results of SEC-MALS experiments showing that monomer is the main species for RUVBL1, whereas the hexamer is the major species for RUVBL2. When RUVBL1 and RUVBL2 were mixed at 1:1 molar ratio, hexamers, dimers, and monomers were observed by SEC-MALS at all tested concentrations (Figure 2A, and Table S1). Interestingly, the

appearance of dimeric species suggested the formation of RUVBL1-RUVBL2 heterodimers. As noticed for RUVBL2, increasing the concentration of the RUVBL1/2 complex promoted oligomerization (Figure 2A).

We also used the recently developed mass photometry technology (Young et al., 2018) to characterize the oligomeric behavior of RUVBL1/2 in solution (Figure 2B). Even at low concentrations of 0.2 μ M, RUVBL1/2 displayed primarily hexameric species and, to a lower extent, dimers, monomers and double-hexamers. Analytical SEC experiments showed that RUVBL1 readily associates with RUVBL2 to form high molecular mass species, even at low concentrations (Figure S2A). The addition of nucleotides did not affect the solution behavior of either RUVBL1, RUVBL2 and RUVBL1/2 complex (Figure S2A). However, the presence of a tag at the N-terminus of RUVBL1 or RUVBL2 affected the hydrodynamic behavior of the individual proteins (Figure S2C) and the heterocomplex (Figure S2D). Electron micrographs of RUVBL1/2 (Figure S2D) clearly showed a tendency to form double-hexamers when one of the subunits was N-terminally tagged. This is similar to what we observed with the yeast proteins (Cheung et al., 2010). Therefore, all of our experiments were performed using untagged RUVBL1 and RUVBL2.

Next, the solution structure and conformation of RUVBL proteins were studied by SAXS. Shown in the Figure 2C are the scattering profiles of RUVBL2 and RUVBL1/2 at two concentrations. Inspection of the curves by Guinier approximation (Figure 2C, inset) and dimensionless Kratky analysis (Figure S2E) suggested that samples were well-behaved (Table S2), with RUVBL1/2 complex presenting slightly higher flexibility than RUVBL2, likely due to DII dynamics. Using merged scattering profiles, distance distribution functions $P(r)$ were generated, revealing similar dimensions for RUVBL2 and RUVBL1/2 (Figures 2D,E and Table S2).

To obtain further insights into RUVBL conformations in solution, theoretical $P(r)$ were

calculated from the published high-resolution 3D structures and compared to the experimental SAXS data (Figures 2D,E). It was intriguing to observe that the DII domain can adopt either an up or down conformation depending on whether DII is close or away from the AAA+ core, respectively (Figure 2F). Comparison between the experimental $P(r)$ of RUVBL2, RUVBL1/2 and the theoretically derived $P(r)$ from the different X-ray structures (Figure 2D,E) suggests that, in solution, hexameric RUVBL2 and hetero-hexameric RUVBL1/2 have DII in the up conformation. Furthermore, three-dimensional CORAL models (Petoukhov et al., 2012) were constructed for both RUVBL2 (Figure 2D) and RUVBL1/2 (Figure 2E). All of the ring-like structures displayed DII adopting the up conformation. The modeling strategy showed an excellent fit with experimental data for both proteins (Figure S2F, Table S2).

Taken together, these experiments unambiguously demonstrate that RUVBL1 is mainly monomeric, whereas RUVBL2 and RUVBL1/2 are mostly hexamers in solution. Moreover, the DII domains in apo RUVBL2 and apo RUVBL1/2 hexamers adopt the up conformation.

Solution structure and dynamics of RPAP3 and RPAP3-PIH1D1 complex

Next, we characterized the solution behavior of RPAP3 iso1 (Figure 1A; also referred to here as RPAP3), PIH1D1 and the RPAP3-PIH1D1 complex. We purified recombinant RPAP3 and RPAP3-PIH1D1 in their folded state (Figure S1) and carried out SEC-MALS experiments varying protein concentration from 1 to 3 mg/mL (13.2 to 39.6 μ M protomers of RPAP3 and 9.3 to 27.8 μ M protomers of RPAP3-PIH1D1). RPAP3 behaved as a monomer, while RPAP3-PIH1D1 formed heterodimers in solution (Figure 3A, Table S1). We also purified PIH1D1 (Figure S1), though due to solubility issues, we were not able to reach high concentrations, precluding accurate molecular mass determinations. However, the chromatographic profile of PIH1D1 showed three peaks, suggesting a behavior composed of multiple oligomeric species in solution (Figure 3A).

The molecular masses of RPAP3, RPAP3-PIH1D1 and PIH1D1 were also investigated by mass photometry (Figure 3B). RPAP3 displayed molecular mass distribution with two peaks, a main one corresponding to monomers and a minor one corresponding to dimers. The monomer molecular mass is similar to that obtained by analytical ultracentrifugation sedimentation velocity experiments (Figure S3A). RPAP3-PIH1D1, on the other hand, displayed a molecular mass distribution consisting mainly of heterodimers (Figure 3B). For PIH1D1, although close to the limit of the detection of the instrument, mass photometry revealed at least three peaks corresponding to monomers, dimers, and tetramers (Figure 3B).

The structures of the individual domains of RPAP3 have been solved (Henri *et al.*, 2018a; Horejsi *et al.*, 2014; Martino *et al.*, 2018; Maurizy *et al.*, 2018; Pal *et al.*, 2014), however the RPAP3 ND remains largely unknown. To gain information about this domain, we initially performed a predictive analysis using PSIPRED, DISOPRED and MARCOIL servers (Figure S3B). A region comprising ~50 residues of RPAP3 ND was found to be α -helix-prone, correlating with a strong likelihood for coiled-coil formation. A high disorder index was observed for the rest of the domain (~65-75 residues). We then purified recombinant RPAP3 ND (Figure 1A) and submitted it to structural analyses. Far-UV circular dichroism revealed a spectral profile characteristic of disordered proteins with some α -helical content, with minima at ~202 nm and ~222 nm (Figure S3C). Addition of 4 M of GdnHCl to RPAP3 ND caused loss of signal in the ~222 nm band, leading to the appearance of a ~218 nm peak (Figure S3C), suggesting that PII-type helical structures may be formed under this condition (Chemes *et al.*, 2012). When exposing RPAP3 ND to increasing temperatures, we observed a loss of signal in its circular dichroism spectrum (Figure S3D). Nonetheless, we noticed loss of protein due to aggregation and further inspection of its spectra revealed no substantial changes in the RPAP3 ND profile (Figure S3D, inset). Intrinsic fluorescence emission using Trp residues as probes revealed that W31 and W93 are fully exposed to the solvent, confirming the intrinsically

disordered nature of RPAP3 ND (Figure S3E). Moreover, the hydropathy index of this domain was compatible with those of intrinsically disordered proteins (Figure S3F).

RPAP3 is a large protein containing extensive intrinsically disordered regions e.g., ND and IDR, in addition to well-folded domains (Figures 1A, S1 and S3B,C), which makes it difficult to determine the structure of the full-length protein by X-ray crystallography or NMR. Therefore, we made use of SAXS to determine the structure and dynamics of the full-length RPAP3 and RPAP3-PIH1D1. The X-ray scattering curves of RPAP3 and RPAP3-PIH1D1 are depicted in Figure 3C. Guinier approximation showed that samples were monodisperse (Figure 3C, inset) and dimensionless Kratky analysis revealed that RPAP3 is quite flexible in solution, while RPAP3-PIH1D1 tends to be slightly less flexible (Figure S3G).

$P(r)$ functions were generated for RPAP3 and RPAP3-PIH1D1 (Figure 3D), displaying single peaks smoothly decaying to long distances, as those for elongated and flexible molecules (Kikhney and Svergun, 2015); RPAP3 displayed smaller size and dimensions than RPAP3-PIH1D1 complex (Table S2). Using dummy atoms (DA), *ab initio* models were generated (Figure S3H; Table S2, DAM). RPAP3 and RPAP3-PIH1D1 DA models have similar elongated shapes in solution (Figure 3E), albeit the latter presented extra DA occupancy that can be attributed to the presence of PIH1D1 (Figure 3E, outlined by a black dashed ellipse). Since samples are conformationally polydisperse, we were not able to precisely determine the localization of RPAP3 domains nor of PIH1D1 in the DA models. To overcome this issue, we employed the Ensemble Optimization Method (EOM) to characterize the dynamics of RPAP3 in solution. Using the crystal structures of TPR1 (Pal *et al.*, 2014), TPR2 (Henri *et al.*, 2018a) and CD (Maurizy *et al.*, 2018) of RPAP3, the ensemble containing conformers best representing the experimental SAXS curve were selected from a pool of random conformers (Figure 3F, S3I; Table S2, EOM). The analysis indicates that despite being a very dynamic protein, RPAP3 adopts more compact conformations rather than fully stretched ones.

The EOM strategy was not applicable to RPAP3-PIH1D1 complex due to intrinsic limitations of the methodology, yet we explored RPAP3-PIH1D1 SAXS data further using a combination of rigid-body modelling by CORAL followed by models clustering based on similarity using DAMCLUST. RPAP3 domains used for EOM were applied in CORAL, in addition to PIH1D1 PIH1 (Horejsi *et al.*, 2014) and CS (Henri *et al.*, 2018a) domains. Contacts between PIH1D1 and RPAP3 were imposed according to interacting interfaces identified in this work and presented below. After generation of 50 rigid-body structures, we clustered them to 7 final representative structures (Figure 3G, S3I; Table S2, CORAL) and, much like RPAP3, more compact structures instead of stretched ones were observed.

In summary, RPAP3 is a monomeric, elongated, and dynamic protein containing an intrinsically disordered ND and adopts more compact conformations. PIH1D1 binds to RPAP3 at a 1:1 molar ratio, forming a compact complex, and seems to partially restrict RPAP3 IDR flexibility.

Mapping the RPAP3 and PIH1D1 interacting interfaces

In our effort to determine the quaternary assembly of R2TP, we subsequently sought to identify the binding interfaces among the R2TP subunits. The interaction between RPAP3 and PIH1D1 was initially investigated by yeast 2-hybrid assays (Figures 4A and S4A). Full-length RPAP3 (RPAP3 iso1₁₋₆₆₅) interacted with full-length PIH1D1 (PIH1D1₁₋₂₉₀), but not with the PIH1D1 construct lacking the last 10 amino acid residues of its CS domain (PIH1D1₁₋₂₈₀). Pull-down assays further confirmed that the deletion of PIH1D1 residues from 281 to 290 disrupted PIH1D1 binding to RPAP3 (Figure 4A).

A comparison between RPAP3 isoforms revealed that amino acid residues from 396 to 429 in iso1 are missing in iso2, which does not interact with PIH1D1 (Yoshida *et al.*, 2013) (Figure 1A). In addition to that, our yeast 2-hybrid assays showed that RPAP3 iso1₁₋₅₆₅ and

RPAP3 iso1₁₋₄₆₅ interacted with PIH1D1₁₋₂₉₀, but RPAP3 iso1₁₋₄₁₅ and RPAP3 iso1₁₋₃₉₀ failed to do so (Figures 4A and S4A). Considering these results and differences between RPAP3 iso1 and iso2, led us to hypothesize that the RPAP3 iso1 region spanning residues from 416 to 429 contains the PIH1D1-binding site. Therefore, pull-down experiments were carried out with RPAP3 iso1₁₋₄₃₀ and RPAP3 iso1₁₋₄₁₅, as well as RPAP3 iso1₁₋₃₉₀ as a negative control since it lacks almost the entire IDR (Figure 1A). We observed that RPAP3 iso1₁₋₄₃₀ was pulled-down by PIH1D1₁₋₂₉₀, whereas RPAP3 iso1₁₋₄₁₅ and RPAP3 iso1₁₋₃₉₀ were not, confirming that the PIH1D1-binding region on RPAP3 iso1 is contained within residues 416 and 429 of its IDR. In addition, XL-MS experiments with the R2TP complex identified cross-linked peptides between RPAP3 IDR and PIH1D1 CS (Figure S4B and Table S3).

Altogether, RPAP3 iso1 IDR residues from 416 to 429 are required for binding to PIH1D1 and the deletion of the last 10 residues in β 7 strand of PIH1D1 CS disrupts its association with RPAP3 iso1 (Figures 1B).

Mapping the PIH1D1 and RUVBL1/2 interacting interfaces

Next, the association between RUVBL1/2 and H7-PIH1D1 was investigated using pull-down assays. Full length PIH1D1₁₋₂₉₀ interacted with full length RUVBL1₁₋₄₅₆/2₁₋₄₆₃ to form the R2P complex (Figure 4B – 1st panel from top). To identify where RUVBL1/2 binds on PIH1D1, a series of progressive deletions of 10 residues were made at the PIH1D1 C-terminus. PIH1D1₁₋₂₈₀, PIH1D1₁₋₂₇₀, and PIH1D1₁₋₂₆₀ constructs all interacted with RUVBL1₁₋₄₅₆/2₁₋₄₆₃ in a similar manner (Figure 4B – 2nd to 4th panels from top). However, PIH1D1₁₋₂₅₀ and PIH1D1₁₋₂₄₀ interacted significantly less with RUVBL1₁₋₄₅₆/2₁₋₄₆₃ (Figure 4B – 5th and 6th panels from top), suggesting that the binding site consists mainly of PIH1D1 residues from 251 to 259 in the CS domain (Figure 1B). Controls to rule out unspecific RUVBL1/2 binding to beads are shown in Figure S4C.

To determine which RUVBL protein binds to PIH1D1, H₇-PIH1D1₁₋₂₉₀ was used to pull-down either RUVBL1₁₋₄₅₆ or RUVBL2₁₋₄₆₃; H₇-PIH1D1₁₋₂₉₀ only interacted with RUVBL1₁₋₄₅₆ (Figure 4C). To determine where PIH1D1 bound on RUVBL1, the complex consisting of a RUVBL1 mutant lacking DII_{ext} (RUVBL1 Δ ₁₂₆₋₂₃₄) and RUVBL2₁₋₄₆₃ was made and pulled-down with H₇-PIH1D1₁₋₂₉₀ (Figure 4D), but no interaction was observed. Controls for unspecific RUVBL1, RUVBL2 and RUVBL1 Δ ₁₂₆₋₂₃₄/RUVBL2₁₋₄₆₃ binding to beads are shown in Figure S4C. Curiously, we did not observe cross-linked peptides between RUVBL proteins and PIH1D1 protein in XL-MS experiments with R2TP (Fig. S4B).

Hence, residues from 251 to 259 in the β 5 strand of PIH1D1 CS domain bind to DII_{ext} of RUVBL1 within the RUVBL1/2 complex (Figure 1B).

Mapping the RPAP3 and RUVBL1/2 interacting interfaces

To determine the RPAP3 domain interacting with RUVBL proteins, full-length RPAP3 iso1, a RPAP3 mutant lacking ND (RPAP3 iso1₁₂₅₋₆₆₅), and a RPAP3 mutant lacking CD (RPAP3 iso1₁₋₅₄₀) were used to pull-down RUVBL1₁₋₄₅₆/2₁₋₄₆₃. The deletion of RPAP3 CD disrupted complex formation with RUVBL1/2 (Figure 4E). Next, to determine which RUVBL protein RPAP3 associates with, both RPAP3 iso1₁₋₆₆₅ and RPAP3 iso2₁₋₆₃₁ were used to pull-down the individual RUVBL proteins. Both isoforms pulled-down RUVBL1₁₋₄₅₆ and RUVBL2₁₋₄₆₃ (Figures 4F and S5A). To verify this further, the RPAP3 iso1 CD (RPAP3 iso1₅₄₀₋₆₆₅) was used to pull-down individual RUVBL proteins. Unexpectedly, RPAP3 iso1₅₄₀₋₆₆₅ only interacted with RUVBL2 (Figure 4G), suggesting the presence of a second binding site through which RUVBL1 would interact with RPAP3. There was no unspecific binding observed of RUVBL1₁₋₄₅₆/RUVBL2₁₋₄₆₃, RUVBL1₁₋₄₅₆, and RUVBL2₁₋₄₆₃ to beads (Figure S4C). Note that XL-MS experiments did not show cross-linked peptides between RPAP3 CD and RUVBL proteins (Figure S4B), likely due to the lack of appropriate primary amines within the allotted distance

or orientation to allow for cross-linking.

In the recently published cryo-EM structures of the human R2TP, RPAP3 CD was seen interacting with RUVBL2 DIII domain, whereas RPAP3 ND and TPR domains, together with PIH1D1, were observed near the DII domains of the RUVBL proteins (Martino *et al.*, 2018; Munoz-Hernandez *et al.*, 2019). Indeed, our R2TP XL-MS experiments found RPAP3 ND, TPR1/2 and IDR peptides cross-linked with both RUVBL1 and RUVBL2 DII_{ext} (Figure S4B and Table S3). Therefore, we wondered if RPAP3 would bind the DII of RUVBLs. So, RPAP3 was used to pull-down RUVBL proteins lacking the DII_{ext} (RUVBL1 Δ 126-234 and RUVBL2 Δ 133-238). RPAP3 iso1₁₋₆₆₅ interacted with RUVBL2 Δ 133-238 but not RUVBL1 Δ 126-234 (Figure 4H). These results suggest that, while the RPAP3 CD binds to RUVBL2, an additional RPAP3 region interacts with RUVBL1 DII_{ext}.

To narrow down the binding regions between RUVBL1 and RPAP3, we removed ND and TPR domains of RPAP3 iso1 (RPAP3 iso1₃₈₅₋₆₆₅) and iso2 (RPAP3 iso2₃₈₅₋₆₃₁) and pulled-down full-length RUVBL1 and RUVBL2. In the presence of the RPAP3 iso1 and iso2 IDR, interactions with both RUVBL1 and RUVBL2 were detected (Figure 4I and Figure S5B), revealing that the second binding site was located within RPAP3 IDR. Global sequence alignment was done with RPAP3 to determine conserved amino acids in the IDR, and two regions were identified (Figure 4J). The first one encompasses amino acid residues from 430 to 441 and coincides with the RPAP3 iso1 region co-crystallized with PIH1D1 (Henri *et al.*, 2018a), forming two β strands. The second one is formed by amino acid residues from 492 to 500 and is predicted to also form a β strand. Not only the structures of these two regions are similar but also their amino acid compositions, with both regions containing 5 hydrophobic, 3 positively charged and 1 or 2 negatively charged residues at the end (Figure 4J). We then deleted these regions to verify if they corresponded to putative RUVBL1 binding interfaces. Two RPAP3 constructs, one corresponding to the deletion of the 430 to 441 region (RPAP3

iso1₄₄₂₋₆₆₅) and one to the 492 to 500 region (RPAP3 iso1_{385-665/Δ492-500}), were tested and both interacted with RUVBL1₁₋₄₅₆ and with RUVBL2₁₋₄₆₃ (Figure S5C). Interestingly, when the deletions of the two regions were combined in the RPAP3 iso1_{442-665/Δ492-500} construct, RPAP3 iso1 IDR was no longer observed to bind to RUVBL1₁₋₄₅₆, while the binding to RUVBL2₁₋₄₆₃ was preserved due to the presence of the CD (Figure 4J). In agreement with these results, XL-MS data revealed that the RPAP3 K495 residue crosslinks with RUVBL1 and RUVBL2 DII_{ext} peptides within the R2TP complex (Figure S4B and Table S3).

Our results demonstrate that RPAP3 iso1 and iso2 form complexes with RUVBL1/2 via two binding sites. The first is through RPAP3 CD, which binds to RUVBL2; the second one is through two regions in IDR, 430 to 441 and 492 to 500, that bind to RUVBL1 DII_{ext} and are proposed to form β strands (Figure 1B).

The assembly of human R2TP

After mapping the interactions among the R2TP proteins, the assembly mechanism of the entire R2TP complex was then investigated. Initially, bacterial cell lysates co-expressing RPAP3 iso1₁₋₆₆₅-PIH1D1₁₋₂₉₀ or RUVBL1₁₋₄₅₆/2₁₋₄₆₃ were mixed and purified, which allowed us to pull-down the R2TP complex (Figures 5A and S6A, top panels). When the same approach was used but employing RPAP3 iso2₁₋₆₃₁, PIH1D1₁₋₂₉₀ was not part of the complex anymore (Figure 5A, bottom panel). On the other hand, when PIH1D1₁₋₂₉₀ was used to pull-down the complex, RPAP3 iso2₁₋₆₃₁ was absent from it (Figure S6A, bottom panel).

We showed that PIH1D1 interacts with RUVBL1/2 (Figure 4B) and, taking into account the human R2TP structures (Martino *et al.*, 2018; Munoz-Hernandez *et al.*, 2019), we wondered if the presence of the RPAP3 ND, TPR1 and TPR2 in the vicinity of the RUVBLs DII could be hindering the direct binding of PIH1D1 to RUVBL1/2. To investigate this possibility, RPAP3 iso1₃₈₅₋₆₆₅ and RPAP3 iso2₃₈₅₋₆₃₁, which only have the IDR and CD, were

co-expressed with PIH1D1₁₋₂₉₀ and mixed with co-expressed RUVBL1_{1-456/21-463}. Even in the absence of ND and TPR domains, RPAP3 iso1₃₈₅₋₆₆₅ formed a complex with PIH1D1₁₋₂₉₀ and RUVBL1_{1-456/21-463} (Figures 5B and S6B, top panel); however, RPAP3 iso2₃₈₅₋₆₃₁ did not (Figures 5B and S6B, bottom panel). These results suggest that RPAP3 iso2 and PIH1D1 may compete for RUVBL1/2 binding.

The above results lead us to propose that PIH1D1, in fact, does not directly interact with RUVBL1/2 within the R2TP complex. PIH1D1 interaction with RUVBL1/2 seems to be mediated by RPAP3 iso1. In agreement with this hypothesis, XL-MS data did not detect cross-linked peptides between PIH1D1 and RUVBL1/2 in R2TP (Figure S4B and Table S3). To confirm this, pull-down experiments were carried out using RPAP3 iso1 as bait and RUVBL1, RUVBL2, and the RPAP3-binding defective mutant of PIH1D1, PIH1D1₁₋₂₈₀, as preys. RPAP3 iso1₁₋₆₆₅ pulled-down RUVBL1_{1-456/21-463} but not PIH1D1₁₋₂₈₀ (Figure 5C), thereby confirming that PIH1D1 cannot directly bind to RUVBL1/2 when RPAP3 is bound to the ATPases. Deletion of the DII_{ext} domains of RUVBLs, RUVBL1_{Δ126-234} and RUVBL2_{Δ133-238}, did not interfere with the formation of the R2TP complex (Figure 5D, top panel). However, the replacement of PIH1D1₁₋₂₉₀ by PIH1D1₁₋₂₈₀, which cannot bind RPAP3 (Figure 4A), showed impairment of the R2TP formation (Figure 5D, bottom panel). Therefore, instead of establishing a direct contact with RUVBL1/2, PIH1D1 depends on RPAP3 iso1 to be part of the R2TP complex.

The above experiments clearly establish that PIH1D1 cannot be part of the R2TP if not bound to RPAP3. Subsequently, we wondered what elements in RPAP3 might be responsible for disrupting the association between PIH1D1 and RUVBL1/2. We performed pull-down experiments using RPAP3 iso1₅₄₀₋₆₆₅ (CD), PIH1D1₁₋₂₉₀ and RUVBL1_{1-456/21-463}. When RPAP3 iso1₅₄₀₋₆₆₅ was used as bait, it only pulled-down RUVBL1/2 but not PIH1D1 (Figure 5E). Reverse pull-down, using PIH1D1₁₋₂₉₀ as bait, pulled-down RUVBL1/2 but not RPAP3

iso1 CD (Figure S6C), hence, revealing that the mere binding of the RPAP3 CD to RUVBL1/2 blocks PIH1D1 binding and vice versa.

We also tested if the presence of all other RPAP3 iso1 regions, except CD, could affect PIH1D1 binding to RUVBL1/2. Figure 5F depicts the result of the experiment with the RPAP3 construct lacking the CD, RPAP3 iso1₁₋₅₄₀, being used as a bait to pull-down RUVBL1₁₋₄₅₆/2₁₋₄₆₃ and PIH1D1₁₋₂₉₀. The reverse pull-down, using PIH1D1₁₋₂₉₀ as bait instead, is shown in the Figure S6D. Surprisingly, RPAP3 iso1₁₋₅₄₀ and PIH1D1₁₋₂₉₀ were able to interact with each other, but not with RUVBL1₁₋₄₅₆/2₁₋₄₆₃, suggesting that the simple binding of RPAP3 iso1 to PIH1D1 competes with its interaction to RUVBL1/2.

Altogether, these experiments demonstrate that RPAP3 is the central subunit of the R2TP complex, bridging the interaction between RUVBL1/2 and PIH1D1. Additionally, the binding of RPAP3 to RUVBL1/2 blocks the binding of PIH1D1 via two mechanisms: (1) binding of RPAP3 CD to RUVBL1/2 likely by changing the conformation of the DII domain in RUVBL1; and (2) binding of RPAP3 to PIH1D1 likely by blocking the binding site of PIH1D1 for RUVBL1 in the RUVBL1/2 complex.

Stoichiometry of the subunits in the R2TP complex

Despite the recent studies on the human R2TP structure (Martino *et al.*, 2018; Maurizy *et al.*, 2018; Munoz-Hernandez *et al.*, 2019), the number of RPAP3 and PIH1D1 subunits associated with RUVBL1/2 remains a matter of debate. In order to determine the subunit stoichiometry within R2TP, we made use of mass photometry. Increasing concentrations of RPAP3 (0.2-1.6 μ M) were titrated into a fixed amount of RUVBL1/2 (0.2 μ M hexamers) as shown in the Figure 6A. RUVBL1/2 complex alone was mostly hexamers with a small population of double-hexamers. However, upon addition of RPAP3, the double-hexameric species disappeared and RUVBL1/2 hexamers containing 1, 2 and 3 RPAP3 bound appeared. Further addition of

RPAP3, up to a ratio of 8 RPAP3 monomers per RUVBL1/2 hexamer, revealed a gradual increase of species containing 2 and 3 bound RPAP3, with almost complete disappearance of the RUVBL1/2 species containing a single RPAP3 associated.

Next, 0.2-1.6 μ M RPAP3-PIH1D1 complex was titrated into 0.2 μ M RUVBL1/2 hexamers (Figure 6B). When RPAP3-PIH1D1 was added at equimolar ratio to RUVBL1/2, the hexamers associated mostly with 1 or 2 RPAP3-PIH1D1 heterodimers. Increasing RPAP3-PIH1D1 concentrations allowed for the formation of RUVBL1/2 bound to 3 RPAP3-PIH1D1 molecules; however, in contrast to RPAP3 titration (Figure 6A), RUVBL1/2 hexamers bound to 1, 2 and 3 RPAP3-PIH1D1 molecules were equally populated.

The above results clearly indicate that, R2TP and R2T are heterogenous complexes containing different stoichiometries of RPAP3 or RPAP3-PIH1D1 bound to the RUVBL1/2. No usable results were obtained in a similar analysis with PIH1D1 due to the experimental limit of detection and instability of PIH1D1.

The effect of nucleotides on R2TP assembly

Recently, PIH1D1 has been proposed to work as a NEF for RUVBL1/2 based on structural studies, but with no biochemical proof (Munoz-Hernandez *et al.*, 2019). Therefore, we investigated if RPAP3 and PIH1D1 have an impact on the ATPase activity of RUVBL1/2. Initially, the ATPase activities of RUVBL1, RUVBL2, and RUVBL1/2 were measured, and the kinetic parameters are shown in Figure 7A. RUVBL2 has a more robust ATPase activity than RUVBL1, and RUVBL1/2 complex has the highest activity [also refer to (Nano et al., 2020)].

Subsequently, RUVBL1/2 concentration was fixed (2 μ M hexamer) and RPAP3, RPAP3-PIH1D1 and RPAP3₅₄₀₋₆₆₅ (CD) were titrated into it. Only a slight increase in the ATPase activity was observed upon addition of RPAP3 (Figure 7B). No significant effect was

observed upon addition of the RPAP3 CD or RPAP3-PIH1D1 complex. Control experiments showed that RPAP3 constructs and RPAP3-PIH1D1 have negligible or little ATPase activity (Figure 7B) that were subtracted from RUVBL1/2-containing data.

Since RPAP3 and RPAP3-PIH1D1 did not affect the ATPase rates of RUVBL1/2, we wondered if they could affect the binding affinity of RUVBL1/2 for nucleotides instead. To address this question, we made use of a fluorescent ADP analogue (mant-ADP) to determine the apparent dissociation constant (K_d^{app}) for the interaction of nucleotides ATP γ S and ADP with RUVBLs. Mant-ADP fluorescence emission spectra undergoes a blue shift when bound to RUVBL1/2; addition of non-fluorescent nucleotides induced dissociation of mant-ADP from RUVBL's ATP-binding pocket. Subsequently, ATP γ S or ADP were titrated into mant-ADP-bound RUVBL1, RUVBL2, RUVBL1/2, R2TP, R2T and R2P samples to determine the K_d^{app} of RUVBLs for nucleotides, shown in Figure 7C. All tested samples did not show significant differences in K_d^{app} for ADP; however, for ATP γ S, RUVBL1 and RUVBL1/2 samples presented ~2 times less affinity in comparison to RUVBL2, R2TP, R2T and R2P. These results suggest that RPAP3, RPAP3-PIH1D1 and PIH1D1 do not significantly affect the affinity of RUVBL1/2 for nucleotides.

Next, using the sensitivity of mant-ADP to the physical-chemical properties of its surrounding, i.e. the spectral shift observed when mant-ADP is free (polar environment) versus protein-bound (hydrophobic environment), we analyzed the solvent accessibility of the ATP-binding pockets of RUVBLs. Figure 7D displays $\langle\lambda\rangle$ -values for RUVBL-bound and unbound mant-ADP. $\langle\lambda\rangle$ refers to spectral center of mass (see methods). R2TP-bound mant-ADP exhibited lowest $\langle\lambda\rangle$ -values, indicating that the nucleotide-binding pocket is most protected from the polar environment in these complexes. Importantly, these results indicate that the binding of RPAP3 and RPAP3-PIH1D1 to RUVBL1/2 shields the ATP-binding pocket instead of opening it to the solvent, as earlier proposed in previous work (Munoz-Hernandez *et al.*,

2019).

Subsequently, we examined if nucleotides affected the complex composition. To do so, R2TP, R2T, and R2P complexes were immobilized on Co^{2+} beads through His-tagged RPAP3 or PIH1D1 and then incubated with buffer containing ATP, ADP, or no nucleotide. Released proteins were then visualized by Western Blot. None of the complexes disassembled upon nucleotide addition (Figure 7E-G), except for the RUVBL1/2-PIH1D1 complex (Figure 7H).

Taken together, these results demonstrate that RPAP3 and RPAP3-PIH1D1 do not affect RUVBL1/2 ATPase activity nor their binding affinity for nucleotides, and that only the R2P complex falls apart upon nucleotide binding to RUVBL1/2. In addition, ATP hydrolysis seems to be the rate limiting step for RUVBL1/2 activity, since the K_M is significantly higher than the K_d^{app} (Figure 7A,C).

***In vivo* implications to R2TP complex assembly**

Our *in vitro* data indicates the presence of R2T and R2P complexes in addition to the R2TP. Using pull-downs of RPAP3 iso1 in *PIH1D1* deleted cells and of PIH1D1 in *RPAP3* deleted cells, we show that R2T and R2P can also be observed *in vivo*, respectively (Figure 8A,B). Furthermore, the pull-down of RPAP3 iso2 only brings down RUVBL1 and RUVBL2 and not PIH1D1 as expected (Figure 8C).

To further explore the role of the intrinsically disordered RPAP3 ND in substrate recognition, we also performed affinity purification followed by mass spectrometry (AP-MS). Using recombinant purified His₁₂-SUMO-tagged RPAP3 ND, we pulled-down proteins from cell extracts that were then analyzed by MS. Enrichment analysis on the identified proteins using DAVID server (Huang et al., 2009a; b) showed that RPAP3 ND preferentially binds to proteins containing Armadillo (ARM) repeats, HSP70 proteins, Calponin homology domain, SEA domains, TPR domain-containing proteins and REJ-like structures (Figure 8D, Table S4).

Of note, most of the domains present in ~70% of the interacting proteins are all α -helical.

Comparison of RPAP3 ND interactors with R2TP interactors retrieved from BioGRID (Figure 8E) shows that TTI2, which has ARM-type repeats, interacts with all four R2TP subunits and with RPAP3 ND, suggesting that TTI2 might be an important component of the R2TP complex.

DISCUSSION

In this work we have combined a series of biophysical and biochemical methods to comprehensively characterize the solution structure of human R2TP subunits and how they interact with one another to assemble the R2TP complex. Our data suggest the presence of three distinct complexes in the cell: R2T (RUVBL1-RUVBL2-RPAP3), R2P (RUVBL1-RUVBL2-PIH1D1), and R2TP (RUVBL1-RUVBL2-RPAP3-PIH1D1).

For the formation of the R2T complex (Figure 9, top panel), we propose that RPAP3 first interacts with RUVBL1/2 AAA+ core via CD, locking RUVBL1/2 in a conformational state where the DIIs are in the ‘up’ position. This conformation blocks the binding of PIH1D1 to RUVBL1/2 and, subsequently, the RPAP3 IDR interacts with RUVBL1 DII_{ext} (Figure 1B) to promote the proper R2T architecture.

In the R2P complex (Figure 9, middle panel) PIH1D1 binds to RUVBL1 mainly via β 5 strand of its CS domain but only in the absence of RPAP3 (Figures 1B, 4B, S7A). In fact, the prior binding of PIH1D1 to RUVBL1/2 abolishes the RPAP3-RUVBL1/2 interaction (Figure S6A-C).

Contrary to what was suggested by the published cryo-EM structures (Martino *et al.*, 2018; Munoz-Hernandez *et al.*, 2019), here we show that, within the R2TP complex, PIH1D1 does not interact directly with RUVBL1/2 and does not act as a NEF for RUVBL1/2. We also found that RPAP3 and RPAP3-PIH1D1 have no significant effect on the ATPase activity of

RUVBL1/2 (Figure 7B). RPAP3 is the link connecting PIH1D1 to and positioning it in the R2TP complex through: (1) the anchoring of the RPAP3 CD on the apical surface of the RUVBL1/2, and (2) the interaction of the residues 430-441 and 492-500 in the RPAP3 IDR with RUVBL1 DII_{ext} (Figures 1B). This places PIH1D1 on the lower side of the RUVBL1/2 hexamer (Figure 9, bottom panel).

The association of PIH1D1 with RPAP3 is dependent on the very C-terminus of PIH1D1 CS domain and residues 416-429 at the beginning of RPAP3 iso1 IDR (Figures 1B and 4A), which is in partial agreement with previously published data (Henri *et al.*, 2018a; Martino *et al.*, 2018). Henri and colleagues (Henri *et al.*, 2018a) had shown that the binding of PIH1D1 to RPAP3 involves extensive contacts between the two proteins, whereby the RPAP3 IDR residues 431-441 loop around the CS domain of PIH1D1 forming intermolecular β strands (Figure S7B). In contrast, we show that residues 416-429 of RPAP3 iso1 IDR are, in fact, responsible for binding PIH1D1. In our study, the RPAP3 IDR region reported to loop around PIH1D1 CS domain is completely dispensable for the heterodimer formation. This region is also present in the RPAP3 iso2, which does not bind to PIH1D1. The difference between our data and Henri *et al.* (Henri *et al.*, 2018a) (Figure S7) might be due to spurious interactions induced by crystal packing forces stabilizing the IDR of RPAP3 and the disordered C-terminal end of PIH1D1.

R2TP species containing one, two and three RPAP3-PIH1D1 bound seem to co-exist in equilibrium (Figure 6). These observed stoichiometries, added to the RPAP3 flexibility, allow us to hypothesize that one RPAP3 and PIH1D1 in the R2TP complex may act to interact with R2TP clients, while the other two PIH1D1 subunits in complex with RPAP3 recruit other clients to R2TP. This would allow the different clients to interact and render R2TP a highly dynamic assembly platform for quaternary structure formation.

ACKNOWLEDGEMENTS

TVS was supported by a CNPq-Brazil (202192/2015-6), a SHRF and a CIHR postdoctoral fellowships. SA was supported by the Royal Golden Jubilee PhD Program of The Thailand Research Fund (PHD/0084/2553). CC was supported by FAPESP (2016/01603-9). YQM is supported by a fellowship from the Centre for Pharmaceutical Oncology (University of Toronto). VB was supported by an Ontario Graduate Scholarship and the NSERC Postgraduate Scholarship-Doctoral award and a Jaro Sodek Award – Ontario Student Opportunity Trust Fund fellowship from the Department of Biochemistry at the University of Toronto. GY was supported by a Zvi and Ofra Meitar Magdalen Graduate Scholarship. VT was supported by Mahidol University research grant and the Thailand Research Fund (IRN60W0004). PK was supported by an ERC Consolidator grant (PHOTOMASS 819593). This work was supported by a CIHR Project grant (PJT-173491) to WAH, and by Global Affairs Canada and CAPES (99999.004913/2015-09; Brazil) to WAH and CHIR. This study was partially supported by FAPESP (2015/15822-1, 2012/01953-9, 2016/05019-0) and a CNPq to LRSB who also holds a research fellowship from CNPq (306943/2015-8, 420567/2016-0). CHIR has research fellowship from CNPq and FAPESP (2012/50161-8; 2017/26131-5). JCB has research fellowship from CNPq and FAPESP (303262/2018-4; 2017/26131-5). MB is supported by a CIHR foundation grant (FDN-154318).

AUTHOR CONTRIBUTIONS

TVS and NN initiated this project with WAH. TVS with the help of YWSC, SA and CC carried out or was involved in most of the experiments. SA was supervised by VT and CC was supervised by LMG. NN did the ATPase assays of Figure 7A and SEC experiments of Figure S2A,C. YQM did the experiments using mammalian cell cultures described in Figure 8A-C.

GY under the supervision of PK carried out the mass photometry experiments of Figure 6. LH, SP and TVS under the supervision of MB did the mass spectrometry experiments of Figure 8D and the XL-MS experiments of Figure S4B. YG under the supervision of CVR did the mass spectrometry experiments of Figure S2B. DRS did the EM experiments of Figure S2D. TVS, VB, YQM, JCB, LRSB, and CHIR contributed to the SAXS experiments. TVS and WAH wrote the first draft of the manuscript. Everyone helped with editing the draft.

DECLARATION OF INTERESTS

The authors declare no competing financial interests. P.K. is a founder, director and shareholder in Refeyn Ltd. G.Y. is a founder, consultant and shareholder in Refeyn Ltd.

FIGURE LEGENDS

Figure 1. Schematics of the R2TP subunits.

(A) Domain arrangement of RUVBL1, RUVBL2, RPAP3 isoforms 1 and 2, and PIH1D1. The indicated domain boundaries are used throughout this work. DI: domain I, DII: domain II, DII_{int}: internal DII, DII_{ext}: external DII, ND: N-terminal domain, TPR: tetratricopeptide repeat-containing domain, IDR: intrinsically disordered region, ND: N-terminal domain, CD: C-terminal domain, PIH1: protein interacting with Hsp90-1 domain, CS: CHORD-containing proteins and SGT1 domain.

(B) Mapping of R2TP interacting interfaces as determined in this work. Solid lines represent interactions observed in the R2TP and R2T complexes. Dashed line indicates the interaction observed in the R2P complex.

Figure 2. Solution structure of RUVBL1 and RUVBL2.

(A) Molecular mass determination of RUVBL1, RUVBL2 and RUVBL1/2 complex using SEC-MALS. Molecular masses of 50 kDa, 100 kDa and 300 kDa are indicated as references (dashed gray lines). See also Table S1 and Figure S2A-D.

(B) Molecular mass distribution of the RUVBL1/2 complex by mass photometry. The observed oligomeric species are indicated.

(C) SAXS profiles of RUVBL2 and RUVBL1/2 complexes (empty circles) at 0.85 mg/mL (Low) and 1.7 mg/mL (High), and their respective GNOM fits (solid lines). Guinier approximation analyses are shown in the inset. Data are shown as empty circles and their respective linear fits are displayed as solid lines.

(D) Experimental P(r) function of RUVBL2 and comparison with theoretical P(r) of RUVBL1 hexamer (R1), RUVBL2 hexamer (R2) and RUVBL2 hexamer lacking DII_{ext} (R2_{ΔDIIext}).

Structures shown on the left side. On the right side, the CORAL model of RUVBL2 is displayed. The AAA+ core and DII_{int} are colored in blue; DII_{ext} is shown in red. See also Table S2 and Figure S2E,F.

(E) Experimental P(r) of RUVBL1/2 complex shown in comparison with theoretical P(r) of RUVBL1/2 double-hexamer (R1/2 2x6-mer), RUVBL1/2 hexamer in the INO80-bound conformation (R1/2), and RUVBL1 hexamer (R1). Displayed on the right is the RUVBL1/2 CORAL model. AAA+ cores and DII_{int} of RUVBL1 (yellow) and RUVBL2 (blue) are shown; RUVBL1 DII_{ext} and RUVBL2 DII_{ext} are colored in green and red, respectively. See also Table S2 and Figure S2E,F.

(F) Surface representation of RUVBL hexamers with DII_{ext} in ‘up’ (PDB ID: 2C9O) and ‘down’ (PDB ID: 5OAF) conformations. The AAA+ core and DII_{int} are displayed in green; DII_{ext} is shown in blue.

Figure 3. Solution structure of RPAP3 and RPAP3-PIH1D1 complex.

(A) Molecular mass determination of RPAP3 and RPAP3-PIH1D1 complex by SEC-MALS. As reference, molecular masses are indicated by gray dashed lines. PIH1D1 chromatographic profiles are also shown. Peaks of molecular mass standards are indicated by gray dashed horizontal lines. See also Figure S3 and Table S1.

(B) Molecular mass distribution of PIH1D1, RPAP3 and RPAP3-PIH1D1 complex identified by mass photometry. Oligomeric species are indicated by arrows.

(C) SAXS profiles of RPAP3 and RPAP3-PIH1D1 complex (empty circles) and respective GNOM fits (solid lines). Guinier regions are displayed in the inset (data and linear fit are shown as empty circles and solid lines, respectively).

(D) P(r) functions of RPAP3 and RPAP3-PIH1D1 complex.

(E) DA models of RPAP3 and RPAP3-PIH1D1 complex. Refined DA models are shown as

translucent beads while the highest occupancies of DA amongst 20 models are shown as solid beads. In the RPAP3-PIH1D1 DA model, the region with increased DA occupancy is indicated by a dashed ellipse. See also Table S2.

(F) Ensemble optimization analysis of RPAP3. On the left, average R_g and D_{max} distributions of the selected RPAP3 ensembles are shown in comparison to those of a random pool of RPAP3 conformers. Representative RPAP3 conformers are shown on the right. See also Table S2.

(G) CORAL representative models of RPAP3-PIH1D1 complex.

Figure 4. Mapping the interacting interfaces between RPAP3 and PIH1D1, PIH1D1 and RUVBL1/2, and RPAP3 and RUVBL1/2.

(A) Schematics of RPAP3 iso1 and PIH1D1 constructs used for the yeast 2-hybrid are displayed on the left. Interacting and non-interacting proteins are connected by green and red arrows, respectively. The panels on the right show the confirmation of yeast 2-hybrid results by pull-down assays. In the top panel, H₆-PIH1D1₁₋₂₉₀ was used to pull-down RPAP3 iso1 constructs. In the lower panel, H₆-PIH1D1 constructs were used to pull-down RPAP3 iso1₁₋₆₆₅. I is input; FT is flow-through; W is wash; E is elution. See also Figure S4A,C.

(B-I) Determination of the interacting regions among the R2TP proteins. Baits and preys are indicated at the top of the gels. Proteins were detected using the respective antibodies. See text for a detailed explanation. See also Figure S4B.

(J) The sequence logo of two conserved regions identified in the RPAP3 IDR (highlighted in yellow) is shown on top. Hydrophobic, acidic, basic, neutral, and polar amino acids are shown as black, red, blue, purple, and green letters, respectively. Secondary structures of the sequences are given, as well as the properties (+ : positively charged, - : negatively charged, Φ : hydrophobic, ζ : hydrophilic, π : small side-chain) of the most conserved residues. Shown on the bottom are the pull-downs of RUVBL1 or RUVBL2 with H₇-RPAP3 iso1_{442-665/Δ492-500}, i.e.

RPAP3 lacking both of the conserved IDR regions. See also Figure S5.

Figure 5. Mapping the interaction interfaces that drive human R2TP complex assembly.

(A-F) Shown are pulldown assays with baits and preys as indicated at the top of the gels. Proteins were detected using the respective antibodies. See text for more details and Figure S4B,S6.

Figure 6. Stoichiometry of the R2TP complex determined by mass photometry.

(A) Titration of RPAP3 iso1 into 0.2 μ M of RUVBL1/2 hexamers. Molecular mass distributions are shown for each RPAP3 iso1 concentration (solid black lines). The curves were fit to a sum of Gaussian models. The blue dashed lines show the fit for each experimental curve and the red dashed lines show the contribution of each component. Identified macromolecular species and their respective stoichiometries are indicated by arrows.

(B) Same as A, but for titration of the RPAP3 iso1-PIH1D1 complex into 0.2 μ M of RUVBL1/2 hexamers.

Figure 7. ATPase activity of RUVBL1/2-related complexes, and their nucleotide-binding properties.

(A) Kinetic parameters for the ATPase activity of the RUVBL proteins.

(B) Effect of RPAP3 and PIH1D1 on the RUVBL1/2 ATPase activity. The ATP hydrolysis rate of RUVBL1/2 complex (2 μ M hexamer) was evaluated at increasing concentrations (2-12 μ M) of RPAP3 CD, full-length RPAP3 and RPAP3-PIH1D1. Data were normalized to the ATPase rate of RUVBL1/2 complex by itself. The inset shows negligible background ATPase activity for RPAP3 CD, RPAP3 iso 1, and PIH1D1.

(C) Binding affinity of RUVBL proteins for adenosine nucleotides and effects of RPAP3,

PIH1D1 and RPAP3-PIH1D1 on the RUVBL1/2 complex. Titration experiments are shown in the top panel for ATP γ S (left side) and ADP (right side). The bottom panel displays calculated nucleotide K_d^{app} for RUVBLs, R2TP, R2T and R2P complexes.

(D) Analysis of the environment experienced by mant-ADP in the ATP-binding pocket of RUVBL proteins based on experiments performed in **C**. Shown are comparisons of centers of spectral mass for mant-ADP bound and unbound to protein. As reference, the relative degree of solvent exposure is shown on the right.

(E-H) Effect of nucleotides on the assembled R2TP, R2T, and R2P complexes. The complexes were immobilized on Co²⁺ ion-affinity beads via bait proteins and incubated with nucleotides solution. Prey proteins released after nucleotide addition were collected and visualized by western blots.

Figure 8. The presence of R2T and R2P in cells and the identification of RPAP3 ND interacting proteins.

(A) Pull-down of FLAG-tagged RPAP3 iso1 in RPE1 *PIH1D1* knockout cells.

(B) Pull-down of FLAG-tagged PIH1D1 in RPE1 *RPAP3* knockout cells.

(C) Pull-downs of FLAG-tagged RPAP3 iso1 or RPAP3 iso2 proteins expressed in RPE1 cells.

(D) List of proteins interacting with RPAP3 ND identified by AP-MS. Protein domain enrichment analysis was performed using DAVID server and enriched proteins (p-value < 0.05) are highlighted by colored boxes. Figure legend is shown in the bottom panel. See also Table S4.

(E) Venn diagram of RPAP3 ND-interacting proteins identified in this study and R2TP-interacting proteins obtained from BioGRID. Common interactors are shown below each Venn diagram and proteins containing enriched domains are colored as in **A**. Diagrams were obtained using InteractiVenn tool.

Figure 9. Proposed model for the assembly of human R2TP, R2T and R2P complexes.

For visualization purposes, only one RPAP3, RPAP3-PIH1D1 and PIH1D1 are shown bound to RUVBL1/2. See discussion for further details. Representative 3D structures shown were made using the UCSF ChimeraX software (Pettersen et al., 2021). RUVBL1 (PDB ID: 2C9O), RPAP3 and PIH1D1 (hybrid SAXS models from this work) structures were employed. RUVBL1 DI + DIII are shown in yellow and RUVBL2 DI + DIII are shown in blue. DII domains of RUVBL1 and RUVBL2 are colored in orange and dark blue, respectively. See also Figure S7.

STAR*METHODS

KEY RESOURCES TABLE

REAGENT or RESOURCE	SOURCE	IDENTIFIER
Antibodies		
Rabbit polyclonal anti-RUVBL1	Abcam	Cat#ab109330
Rabbit polyclonal anti-RUVBL1	Invitrogen	Cat#PA5-29278
Rabbit polyclonal anti-RUVBL2	Abcam	Cat#ab36569
Rabbit polyclonal anti-RUVBL2	Invitrogen	Cat#PA5-29871
Rabbit polyclonal anti-RPAP3	Invitrogen	Cat#PA5-30816
Mouse monoclonal anti-PIH1D1	Santa Cruz	Cat#sc-101000
Mouse monoclonal anti-FLAG M2	Millipore	Cat#F3165
Mouse monoclonal anti-His tag	Millipore	Cat#05-949
Mouse monoclonal anti-His tag	Bio-Rad	Cat#MCA1396
Bacterial and virus strains		
<i>Escherichia coli</i> LOBSTR BI21(DE3) strain	(Andersen et al., 2013)	N/A
Chemicals, peptides, and recombinant proteins		
Adenosine 5'-triphosphate disodium salt hydrate	Bioshop	Cat#ATP007
Adenosine 5'-diphosphate sodium salt	Sigma-Aldrich	Cat#A2754
Adenosine 5'-(γ -thio)-triphosphate (lithium salt)	Cayman Chemicals	Cat#14957
3-amino-1,2,4-triazole	Sigma-Aldrich	Cat#A8056
Phospho(enol)pyruvic acid monopotassium salt	Sigma-Aldrich	Cat#P7127
NADH disodium salt, trihydrate, reduced	Bio Basic	Cat#NB0642
Pyruvate Kinase/Lactic Dehydrogenase	Sigma-Aldrich	Cat#P0294
2'/3'-O-(N-Methyl-anthraniloyl)-adenosine-5'-diphosphate, triethylammonium salt (mant-ADP)	Jena Bioscience	Cat#JBNU201S
Disuccinimidyl sulfoxide (DSSO)	Thermo Fisher Scientific	Cat#A33545
Tobacco Etch Virus (TEV) protease	Laboratory of Walid Houry, University of Toronto	N/A
Ulp1 protease	(Lee et al., 2008)	N/A
ProteaseMAX	Promega	V2071
Trypsin Gold	Promega	V5280
25 mM Tris-HCl (pH 7.5), 500 mM NaCl	N/A	Buffer A
25 mM Tris-HCl (pH 7.5), 500 mM NaCl, 500 mM imidazole	N/A	Buffer B
25 mM Tris-HCl (pH 7.5), 50 mM KCl, 10% glycerol, 1 mM DTT	N/A	Buffer C
25 mM Tris-HCl (pH 7.5), 500 mM KCl, 10% glycerol, 1 mM DTT	N/A	Buffer D
40 mM Tris-HCl (pH 7.5), 200 mM KCl, 5 mM MgCl ₂ , 1 mM DTT, 10% Glycerol	N/A	Buffer E
25 mM Tris-HCl (pH 7.5), 200 mM NaCl, 10% glycerol	N/A	Buffer F
25 mM Tris-HCl (pH 7.5), 50 mM NaCl	N/A	Buffer G
25 mM Tris-HCl (pH 7.5), 500 mM NaCl	N/A	Buffer H
25 mM Tris-HCl (pH 7.5), 200 mM NaCl	N/A	Buffer I
25 mM Tris-HCl (pH 7.5), 200 mM NaCl, 250 mM imidazole	N/A	Buffer J
20 mM Tris-HCl, pH 7.5, 200 mM KCl, 8 mM MgCl ₂ , 10% (v/v) glycerol	N/A	Buffer K
25 mM Tris-HCl (pH 7.5), 200 mM NaCl, 1 mM DTT, 10% glycerol	N/A	Buffer L
25 mM HEPES (pH 7.5), 200 mM NaCl, 5% glycerol	N/A	Buffer M

50 mM Tris-HCl (pH 7.4), 150 mM NaCl, 1 mM EDTA, 1% Triton X-100	N/A	Buffer N
50 mM Tris-HCl (pH 7.4), 150 mM NaCl, 0.05% Nonidet P-40	N/A	Buffer O
50 mM Tris-HCl (pH 7.4), 150 mM NaCl	N/A	Buffer P
40 mM Tris-HCl (pH 7.5), 200 mM KCl, 5 mM MgCl ₂	N/A	Buffer Q
Deposited data		
Human RUVBL1 structure	(Matias et al., 2006)	PDB ID: 2C9O
Human RUVBL2 structure	(Silva et al., 2018a; Silva et al., 2018b)	PDB ID: 6H7X
Human RUVBL1/2 structure	(Aramayo et al., 2018)	PDB ID: 5OAF
Human RUVBL2ΔDII _{ext} structure	(Petukhov et al., 2012)	PDB ID: 3UK6
Human RUVBL1ΔDII _{ext} /2ΔDII _{ext} complex structure	(Gorynia et al., 2011)	PDB ID: 2XSZ
<i>Chaetomium thermophilum</i> Rvb1/2 complex structure	(Silva-Martin et al., 2016)	PDB ID: 6FM6
Human RPAP3 TPR1 domain	(Pal et al., 2014)	PDB ID: 4CGV
Human RPAP3 TPR2 domain	(Henri et al., 2018a; Henri et al., 2018b)	PDB ID: 6FDT
Human RPAP3 C-domain	(Maurizy et al., 2018)	PDB ID: 6EZ4
Human RPAP3 TPR2-PIH1D1 CS complex structure	(Henri et al., 2018a)	PDB ID: 6GXZ
Human PIH1D1 PIH1 domain	(Horejsi et al., 2014)	PDB ID: 4PSF
Experimental models: Cell lines		
HEK293T	A gift from Dr. Liliana Attisano, University of Toronto	N/A
RPE-1	A gift from Dr. Peter Kim, The Hospital for Sick Children	N/A
RPE-1 <i>RPAP3</i> KO	This paper	N/A
RPE-1 <i>PIH1D1</i> KO	This paper	N/A
Experimental models: Organisms/strains		
<i>Saccharomyces cerevisiae</i> PJ69-4α strain	(James et al., 1996)	N/A
Recombinant DNA		
pACYC RIL (pRIL)	Agilent	N/A
pQLink H7-RUVBL1 ₁₋₄₅₆	This paper	N/A
pQLink H7-RUVBL2 ₁₋₄₆₃	This paper	N/A
p11 H6-RUVBL1 ₁₋₄₅₆	This paper	N/A
p11 H6-RUVBL2 ₁₋₄₆₃	This paper	N/A
pETSUMO2 H12-SUMO-RPAP3 iso1 ₁₋₆₆₅	This paper	N/A
pCOLA Duet-1 RPAP3 iso1 ₁₋₆₆₅ , H6-PIH1D1 ₁₋₂₉₀	This paper	N/A
pQM18 H6-PIH1D1 ₁₋₂₉₀ -H6	(Machado-Pinilla et al., 2012)	N/A
pCOLADuet-1 RPAP3 iso1 ₁₋₆₆₅ , H6-PIH1D1 ₁₋₂₈₀	This paper	N/A
pCOLADuet-1 RPAP3 iso1 ₁₋₄₃₀ , H6-PIH1D1 ₁₋₂₉₀	This paper	N/A
pCOLADuet-1 RPAP3 iso1 ₁₋₄₁₅ , H6-PIH1D1 ₁₋₂₉₀	This paper	N/A
pCOLADuet-1 RPAP3 iso1 ₁₋₃₉₀ , H6-PIH1D1 ₁₋₂₉₀	This paper	N/A
pQLink RUVBL1 ₁₋₄₅₆ -RUVBL2 ₁₋₄₆₃	This paper	N/A
pQLink RUVBL1 ₁₋₄₅₆ , RUVBL2 ₁₋₄₆₃ , H7-PIH1D1 ₁₋₂₉₀	This paper	N/A
pQLink RUVBL1 ₁₋₄₅₆ , RUVBL2 ₁₋₄₆₃ , H7-PIH1D1 ₁₋₂₈₀	This paper	N/A
pQLink RUVBL1 ₁₋₄₅₆ , RUVBL2 ₁₋₄₆₃ , H7-PIH1D1 ₁₋₂₇₀	This paper	N/A
pQLink RUVBL1 ₁₋₄₅₆ , RUVBL2 ₁₋₄₆₃ , H7-PIH1D1 ₁₋₂₆₀	This paper	N/A
pQLink RUVBL1 ₁₋₄₅₆ , RUVBL2 ₁₋₄₆₃ , H7-PIH1D1 ₁₋₂₅₀	This paper	N/A
pQLink RUVBL1 ₁₋₄₅₆ , RUVBL2 ₁₋₄₆₃ , H7-PIH1D1 ₁₋₂₄₀	This paper	N/A
pQLink RUVBL1 ₁₋₄₅₆ , H7-PIH1D1 ₁₋₂₉₀	This paper	N/A

pQLink RUVBL2 ₁₋₄₆₃ , H7-PIH1D1 ₁₋₂₉₀	This paper	N/A
pQLink RUVBL1 _{Δ126-234} , RUVBL2 _{Δ133-238}	This paper	N/A
pQLink RUVBL1 _{Δ126-234} , RUVBL2 ₁₋₄₆₃	This paper	N/A
pQLink RUVBL1 ₁₋₄₅₆ , RUVBL2 ₁₋₄₆₃ , H7-RPAP3 iso1 ₁₋₆₆₅	This paper	N/A
pQLink RUVBL1 ₁₋₄₅₆ , RUVBL2 ₁₋₄₆₃ , H7-RPAP3 iso1 ₁₂₅₋₆₆₅	This paper	N/A
pQLink RUVBL1 ₁₋₄₅₆ , RUVBL2 ₁₋₄₆₃ , H7-RPAP3 iso1 ₁₋₅₄₀	This paper	N/A
pQLink RUVBL1 ₁₋₄₅₆ , H7-RPAP3 iso1 ₁₋₆₆₅	This paper	N/A
pQLink RUVBL2 ₁₋₄₆₃ , H7-RPAP3 iso1 ₁₋₆₆₅	This paper	N/A
pQLink RUVBL1 ₁₋₄₅₆ , H7-RPAP3 iso1 ₅₄₀₋₆₆₅	This paper	N/A
pQLink RUVBL2 ₁₋₄₆₃ , H7-RPAP3 iso1 ₅₄₀₋₆₆₅	This paper	N/A
pQLink RUVBL1 _{Δ126-234} , RUVBL2 _{Δ133-238} , H7-RPAP3 iso1 ₁₋₆₆₅	This paper	N/A
pQLink RUVBL1 ₁₋₄₅₆ , H7-RPAP3 iso1 ₃₈₅₋₆₆₅	This paper	N/A
pQLink RUVBL2 ₁₋₄₆₃ , H7-RPAP3 iso1 ₃₈₅₋₆₆₅	This paper	N/A
pQLink RUVBL1 ₁₋₄₅₆ , H7-RPAP3 iso1 ₄₄₂₋₆₆₅	This paper	N/A
pQLink RUVBL2 ₁₋₄₆₃ , H7-RPAP3 iso1 ₄₄₂₋₆₆₅	This paper	N/A
pQLink RUVBL1 ₁₋₄₅₆ , H7-RPAP3 iso1 _{385-665/Δ492-500}	This paper	N/A
pQLink RUVBL2 ₁₋₄₆₃ , H7-RPAP3 iso1 _{385-665/Δ492-500}	This paper	N/A
pQLink RUVBL1 ₁₋₄₅₆ , H7-RPAP3 iso1 _{442-665/Δ492-500}	This paper	N/A
pQLink RUVBL2 ₁₋₄₆₃ , H7-TEV-RPAP3 iso1 _{442-665/Δ492-500}	This paper	N/A
pQLink H7-RPAP3 iso1 ₁₋₆₆₅ , PIH1D1 ₁₋₂₉₀	This paper	N/A
pQLink H7-RPAP3 iso2 ₁₋₆₃₁ , PIH1D1 ₁₋₂₉₀	This paper	N/A
pQLink H7-RPAP3 iso1 ₃₈₅₋₆₆₅ , PIH1D1 ₁₋₂₉₀	This paper	N/A
pQLink H7-RPAP3 iso2 ₃₈₅₋₆₃₁ , PIH1D1 ₁₋₂₉₀	This paper	N/A
pQLink H7-RPAP3 iso1 ₁₋₆₆₅ , PIH1D1 ₁₋₂₈₀	This paper	N/A
pQLink H7-RPAP3 iso1 ₅₄₀₋₆₆₅ , PIH1D1 ₁₋₂₉₀	This paper	N/A
pQLink H7-RPAP3 iso1 ₁₋₅₄₀ , PIH1D1 ₁₋₂₉₀	This paper	N/A
p11 H ₆ -RUVBL1 ₁₋₄₅₆ WB	This paper	N/A
p11 H ₆ -RUVBL2 ₁₋₄₆₃ WB	This paper	N/A
pCOLADuet-1 RUVBL1 ₁₋₄₅₆ -H ₆ , eXact tag-RUVBL2 ₁₋₄₆₃	This paper	N/A
pETSUMO2 H ₁₂ -SUMO-RPAP3 iso1 ₅₄₀₋₆₆₅	This paper	N/A
pQLink RUVBL1 ₁₋₄₅₆ , H7-RPAP3 iso2 ₁₋₆₃₁	This paper	N/A
pQLink RUVBL2 ₁₋₄₆₃ , H7-RPAP3 iso1 ₁₋₆₃₁	This paper	N/A
pQLink RUVBL1 ₁₋₄₅₆ , H7-RPAP3 iso2 ₃₈₅₋₆₃₁	This paper	N/A
pQLink RUVBL2 ₁₋₄₆₃ , H7-RPAP3 iso2 ₃₈₅₋₆₃₁	This paper	N/A
pCOLADuet-1 RPAP3 iso2 ₁₋₆₃₁ , H ₆ -PIH1D1 ₁₋₂₉₀	This paper	N/A
pQLink RPAP3 iso1 ₃₈₅₋₆₆₅ -FLAG, H7-PIH1D1 ₁₋₂₉₀	This paper	N/A
pQLink RPAP3 iso2 ₃₈₅₋₆₃₁ -FLAG, H7-PIH1D1 ₁₋₂₉₀	This paper	N/A
pQLink RPAP3 iso1 ₅₄₀₋₆₆₅ -FLAG, H7-PIH1D1 ₁₋₂₉₀	This paper	N/A
pQLink RPAP3 iso1 ₁₋₅₄₀ , H7-PIH1D1 ₁₋₂₉₀	This paper	N/A
pOBD2	A gift from Stanley Fields Lab, University of Washington	http://www.fieldslab.org/vector-pobd2.html
pOAD	A gift from Stanley Fields Lab, University of Washington	http://www.fieldslab.org/vector-poad.html
pOBD2 RPAP3 ₁₋₆₆₅	This paper	N/A
pOBD2 RPAP3 ₁₋₅₆₅	This paper	N/A
pOBD2 RPAP3 ₁₋₄₆₅	This paper	N/A
pOBD2 RPAP3 ₁₋₄₁₅	This paper	N/A
pOBD2 RPAP3 ₁₋₃₉₀	This paper	N/A
pOAD PIH1D1 ₁₋₂₉₀	This paper	N/A
pOAD PIH1D1 ₁₋₂₈₀	This paper	N/A

pcDNA5 FLAG-PIH1D1	This paper	N/A
pcDNA5 RPAP3 iso1-3xFLAG	This paper	N/A
pcDNA5 RPAP3 iso1-3xFLAG	This paper	N/A
pcDNA5 FLAG-RPAP3 iso1	This paper	N/A
pcDNA5 RPAP3 iso1-3xFLAG	This paper	N/A
pcDNA5 RPAP3 iso1-3xFLAG	This paper	N/A
pcDNA5 FLAG-RPAP3 iso1	This paper	N/A
Software and algorithms		
ATSAS 2.7.2 package	(Franke et al., 2017)	www.embl-hamburg.de/biosaxs/download.html
ASTRA 7.1.2	Wyatt Technology	https://www.wyatt.com/products/software/astra.html
UCSF ChimeraX 1.1	(Pettersen <i>et al.</i> , 2021)	https://www.cgl.ucsf.edu/chimerax/download.html
Clustal Omega	(Madeira et al., 2019)	https://www.ebi.ac.uk/Tools/msa/clustalo/
Weblogo 3	(Crooks et al., 2004)	http://weblogo.threeplusone.com/
PSIPRED and DISOPRED	(Buchan and Jones, 2019)	http://bioinf.cs.ucl.ac.uk/psipred/
MARCOIL	(Delorenzi and Speed, 2002)	https://bcf.isb-sib.ch/webmarcoil/webmarcoilINFOC1.html
PONDR	Molecular Kinetics Inc.	http://www.pondr.com/
PDBSum	(Laskowski et al., 2018)	http://www.ebi.ac.uk/tornton-srv/databases/cgi-bin/pdbsum/GetPage.pl?pdbcode=index.html
Sedfit	(Schuck, 2000)	http://www.analyticalultracentrifugation.com/download.htm
Origin 7.0	OriginLab Corporation	www.originlab.com
EMAN: Boxer	(Ludtke et al., 1999)	https://blake.bcm.edu/emanwiki/EMAN1
XCalibur 4.1.31.9	Thermo Fisher Scientific	https://www.thermofisher.com/order/catalog/product/OPTON-30965#/OPTON-30965
Proteome Discoverer 2.2	Thermo Fisher Scientific	https://www.thermofisher.com/order/catalog/product/OPTON-30945#/OPTON-30945
xiVIEW	(Graham et al., 2019)	https://xiview.org/xiNET_website/index.php
SEQUEST	(Eng et al., 1994)	http://fields.scripps.edu/yates/wp/?page_id=17
CRAPome	(Mellacheruvu et al., 2013)	https://reprint-apms.org/?q=reprint-home

DAVID	(Huang da <i>et al.</i> , 2009b)	https://david.ncifcrf.gov/
InteractiVenn	(Heberle et al., 2015)	http://www.interactivenn.net/
Other		
Ni Sepharose 6 Fast Flow	GE Healthcare Life Sciences	Cat#17531802
Mono Q 5/50 GL	GE Healthcare Life Sciences	Cat#17516601
HiLoad Superdex 200 16/600 pg	GE Healthcare Life Sciences	Cat#28989335
Superdex 200 Increase 10/300 GL	GE Healthcare Life Sciences	Cat#28990944
Superdex 200 HR10/300 GL	GE Healthcare Life Sciences	Cat#54801-U
HisPur cobalt resin	Thermo Fisher Scientific	Cat#89965
Anti-FLAG M2 magnetic beads	Millipore	Cat#M8823
MiniDAWN TREOS II	Wyatt Technology	Part#WTS2
Optilab T-rEX	Wyatt Technology	Part#WTREX
EnSpire 2300 multilabel reader	Perkin-Elmer	http://www.perkinelmer.com/product/enspire-base-unit-2300-0000
J-810 spectropolarimeter	Jasco	Part#0302-0407A
ProteomeLab XL-A analytical ultracentrifuge	Beckman Coulter	N/A
Fluorolog-3 spectrophotometer	HORIBA	Model#FL3-22
Pilatus 300K detector	Dectris, SAXS1 – Brazilian Synchrotron Light Laboratory	https://www.lnls.cnpe.m.br/saxs1-5/
Mass photometry instrumentation	(Young <i>et al.</i> , 2018)	N/A
High mass Q-TOF-type instrument adapted for a QSTAR CL platform	(Chernushevich and Thomson, 2004; Sobott et al., 2002)	N/A
2010F TEM	JEOL	N/A
Super COOLSCAN 9000 ED	Nikon	https://www.nikonusa.com/en/nikon-products/product-archive/film-scanners/super-coolscan-9000-ed.html
SO-163 film	Kodak	N/A
Tecnai T12	FEI	N/A
4k CCD camera	Gatan	N/A
C-18 TopTip	Glygen	http://www.glysci.com/products/TopTip.html
SpeedVac	Savant	Model#SVC-100H
Luna SCX (50 x 2 mm, 5 µm, 100 Å)	Phenomenex	Part#00B-4398-B0
EASY-nLC 1000	Thermo Fisher Scientific	Cat#LC120
Reprosil-Pur 120 (75 µm I.D., 25 cm length, 3 µm, 120 Å)	Dr. Maisch	C-18-AQ
1100 HPLC	Agilent	N/A
Orbitrap Fusion Tribrid	Thermo Fisher Scientific	Cat#IQLAAEGAAPF ADBMBCX
Nanospray Flex NG	Thermo Fisher Scientific	Cat#ES072
Nano C18 column (10 cm x 75 µm ID, 3 µm, 100 Å)	Laboratory of Mohan Babu, University of Regina	N/A
Orbitrap Elite	Thermo Fisher Scientific	N/A

Äkta Pure	GE Healthcare Life Sciences	Part#29018225
Äkta FPLC	Amersham Biosciences	N/A

RESOURCE AVAILABILITY

Lead contact

Further information and requests for resources and reagents should be directed to and will be fulfilled by Walid A. Houry (walid.houry@utoronto.ca).

Materials availability

Unique/stable reagents generated in this study will be made available upon request as long as in stock; the University of Toronto may require a completed Materials Transfer Agreement.

Data and code availability

No novel code was generated during this work. Raw data are available from the authors upon request. Any additional information required to reanalyze the data reported in this paper is available from the lead contact upon request.

EXPERIMENTAL MODEL AND SUBJECT DETAILS

Escherichia coli cell cultures

E. coli LOBSTR BI21(DE3) strain, carrying mutations in *arnA* and *slyD* genes (Andersen *et al.*, 2013) and transformed with the pRIL (Cam^R) vector (Agilent), was grown at 37°C in Lysogenic Broth (LB) supplemented with 34 µg/mL of chloramphenicol (LB-Clo). LOBSTR BI21(DE3) pRIL cells transformed with Kan^R or Amp^R-containing plasmids were grown in LB-Clo containing 35 µg/mL of kanamycin or 100 µg/mL of ampicillin, respectively.

***Saccharomyces cerevisiae* cell cultures**

S. cerevisiae cells PJ69-4 α strain, genotype MAT α *trp1-901 leu2-3,112 ura3-52 his3-200 gal4 Δ gal80 Δ LYS2::GAL1-HIS3 GAL2-ADE2 met2::GAL7-lacZ* (James *et al.*, 1996), were cultured in YPD medium at 30 °C. When transformed with pOBD2 and pOAD vectors, yeast cells were grown in synthetic defined (SD) medium lacking leucine and tryptophan at 30 °C.

Mammalian cell cultures

HEK293T cells were grown at 37 °C with 5% CO₂ in Dulbecco's Modified Eagle Medium (DMEM) supplemented with 10% fetal bovine serum (FBS) and 100 U/mL penicillin-streptomycin. RPE-1, RPE-1 *RPAP3* KO and RPE-1 *PIH1D1* KO cells were cultured at 37 °C with 5% CO₂ in DMEM/Nutrient Mixture F-12 containing 10% FBS and 100 U/mL penicillin-streptomycin.

METHOD DETAILS

Protein expression and purification

All recombinant proteins were expressed using the *E. coli* LOBSTR strain (Andersen *et al.*, 2013) previously transformed with pACYC RIL (pRIL) (Agilent Technologies), and plasmids used in this work are described in Table S5. Buffer solutions used throughout this work are given in Table S6. Briefly, bacterial cells transformed with the plasmid of interest were initially grown overnight in LB medium at 37 °C. Next day, cells were transferred to fresh LB medium (1-5% culture, v/v) and incubated at 37 °C in an orbital shaker incubator (200 rpm) until OD₆₀₀ = 0.6-0.8. Subsequently, temperature was decreased to 18 °C and IPTG was added to 1 mM final concentration to induce protein expression and, after 15 hours, cells were harvested by centrifugation at 3,000 x g for 10 minutes. Cellular extracts were prepared by resuspending cells in the buffer A (15 mL/liter of culture), followed by sonication on ice. Lysates were spun

down at 12,000 x g for 30 min at 4 °C for cellular debris removal, and supernatants were further purified by immobilized metal affinity chromatography (IMAC), since all recombinant proteins produced were fused to a His-tag.

IMAC was performed as the first purification step for all proteins using Ni Sepharose 6 Fast Flow beads (GE Healthcare Life Sciences) packed into an Econo-column (Bio-Rad). Buffer A was used for washing, whereas the elution step was done with buffer B. Proteins expressed from pQLinkH (Scheich et al., 2007) or p11 (Toronto SGC) had their His-tag cleaved off by tobacco etch virus (TEV), while those expressed from the pET-SUMO plasmid (Invitrogen) had their His-SUMO tag removed by incubation with the Ulp1 protease (Lee *et al.*, 2008). H₆-PIH1D1-H₆ expressed from pRM18 vector (Machado-Pinilla *et al.*, 2012) was kept tagged.

For wild type RUVBL1, RUVBL2 and their mutants, the second and final step of purification consisted of ion exchange chromatography using a Mono Q 5/50 GL column (GE Healthcare Life Sciences) connected to an Äkta Pure system (GE Healthcare Life Sciences). Proteins purified using IMAC were dialyzed against buffer C for 4 hours and submitted to ion-exchange chromatography. The elution was done by a linear gradient from 0% to 100% of buffer D. RUVBL proteins were dialyzed and stored in buffer E.

For structural characterization of RPAP3, PIH1D1 and related constructs were submitted to size exclusion chromatography using a HiLoad Superdex 200 16/600 prep grade (GE Healthcare Life Sciences) equilibrated with buffer F and connected to an Äkta Pure system. For ATPase assays, proteins were dialyzed against buffer G and submitted to an extra purification step of ion exchange in a Mono Q 5/50 GL column (GE Healthcare Life Sciences). Elution was carried out using a linear gradient of buffer H. Samples were dialyzed in buffer E prior to performing the ATPase assays.

***In vitro* pull-down experiments**

All plasmids used for pull-downs throughout this work are described in Table S5. For recombinant protein expression or co-expression, *E. coli* LOBSTR pRIL cells containing the plasmid of interest were grown in 50 mL LB medium at 37 °C in an orbital shaker incubator (200 rpm) until OD₆₀₀ = 0.6-0.8. Subsequently, the temperature was changed to 18 °C and protein expression was induced by 1 mM IPTG final concentration. After 15 hrs, cells were harvested by centrifugation (10 min, 3,000 x g, 4 °C), frozen and kept at -20 °C until use. Bacterial cell lysis was done by sonication after resuspension of the frozen pellets in 2 mL of buffer I. Cellular debris was separated from the soluble fraction of the lysate by centrifugation at 10,000 x g for 10 min at 4 °C. Using 2 mL Econo-columns (Bio-Rad), 100 µL of 50% slurry HisPur Co²⁺ metal affinity beads (Thermo Fisher Scientific) were pipetted in and then washed with 1 mL of buffer I.

The soluble fraction of the lysates was loaded into columns and flowed-through the beads by gravity. Lysates from co-expression were loaded directly into the columns, whereas lysates coming from individually expressed proteins were mixed and incubated for 30 min on ice prior to loading. After loading, beads were washed 8 times with 1 mL of buffer I in order to remove contaminants and unbound proteins. The elution step was performed by adding 100 µL of buffer J. In addition to the eluate, input, flow-through and last wash fractions were collected and analyzed by SDS-PAGE and Western blot. Polyclonal anti-RUVBL1 (Abcam and Invitrogen), anti-RUVBL2 (Abcam and Invitrogen), anti-RPAP3 (Invitrogen) antibodies, and monoclonal anti-PIH1D1 (Santa Cruz) and anti-His tag (Millipore and Bio-Rad) antibodies, were used for immunodetection of proteins.

The dissociation of RUVBL proteins from RPAP3, PIH1D1 and RPAP3-PIH1D1 upon nucleotide binding and/or hydrolysis (Figure 7E-H) was performed following the same procedures described for pull-down experiments, except for the elution step. After the washes,

instead of adding elution buffer containing imidazole, 100 μ L of buffer I containing either 1 mM ATP or ADP were added to beads containing immobilized complexes. Samples were incubated at 37 °C for 30 min and supernatants containing released proteins were collected. Detection of proteins was done by Western blot using the antibodies described above. All *in vitro* pull-down experiments were performed at least in triplicates.

***In vivo* pull-down experiments**

Plasmids used for *in vivo* pull-downs are described in Table S5. Retinal pigment epithelial (RPE-1) cells were transfected with plasmids, and, after 24 hours, cells were washed with PBS. Cell lysis was done in buffer N supplemented with protease inhibitor cocktail (Roche), followed by immunoprecipitation with anti-FLAG M2 magnetic beads (Millipore) according to the manufacturer's protocol. Samples were resolved using SDS-PAGE and visualized by western Blot using PVDF membrane. Antibodies are described above in addition to the monoclonal anti-FLAG M2 antibody (Millipore).

Yeast two-hybrid assay

For the yeast two-hybrid assays, the *S. cerevisiae* PJ69-4 α strain (MAT α *trp1-901 leu2-3,112 ura3-52 his3-200 gal4 Δ gal80 Δ LYS2::GAL1-HIS3 GAL2-ADE2 met2::GAL7-lacZ*) (James *et al.*, 1996), pOBD2 (*TRP1* plasmid) and pOAD (*LEU2* plasmid) plasmids were used (Table S5). Yeast cells containing both pOBD2 and pOAD-derived plasmids were grown overnight at 30 °C in liquid synthetic defined (SD) medium lacking leucine (-L) and tryptophan (-W). Next day, cells were diluted to OD₆₀₀ = 0.1 in SD -L -W -H medium and serial dilutions (from 1 to 1000-fold dilution) were prepared. 5 μ L of the dilutions were spotted on SD -L -W and SD -L -W +100 mM 3-amino-1,2,4-triazole (3-AT, Sigma-Aldrich) plates, which were incubated for 56-72 hrs at 30 °C. These experiments were performed in triplicates.

Analytical size exclusion chromatography (SEC)

SEC experiments were performed at 4 °C using a Superdex 200 HR 10/30 column (GE Healthcare Life Sciences) connected to an Äkta FPLC system (Amersham Biosciences) and equilibrated with buffer E. Proteins were prepared at the desired monomer concentrations, with ATP added, when required, at 1.5 mM final concentration. In general, 200 µL of samples were injected onto the column and their elution profile monitored by absorbance at 280 nm. Fractions of 1 mL were collected, separated on 12% SDS-PAGE gels, and visualized by silver-staining. Protein molecular mass standards consisting of thyroglobulin (669 kDa), apoferritin (443 kDa), β -amylase (200 kDa), alcohol dehydrogenase (150 kDa), bovine serum albumin (66 kDa), carbonic anhydrase (29 kDa), and cytochrome C (12.4 kDa) (GE Healthcare Life Sciences) were used for molecular mass estimations.

Size exclusion chromatography coupled to multi-angle light scattering (SEC-MALS)

SEC-MALS experiments were performed using a Superdex 200 Increase 10/300 column (GE Healthcare Life Sciences) connected to an Äkta Pure system (GE Healthcare Life Sciences) in line with a miniDAWN TREOS II light scattering detector (Wyatt Technology) and an Optilab T-rEX refractive index detector (Wyatt Technology). In all SEC-MALS experiments, 100 µL of protein solution was injected into the size exclusion column equilibrated with buffer I at a 0.5 mL/min flow rate and at 4 °C. Data analysis was done using the ASTRA 7.1.2 software (Wyatt Technology).

ATPase assays

ATPase activity measurements were performed using the ATP/NADH coupled ATPase assay (Norby, 1988). The reactions consisted of 3 mM phosphoenolpyruvate, 0.2 mM NADH, 40

U/mL pyruvate kinase, 58 U/mL lactate dehydrogenase in the buffer K. Proteins of interest and ATP were added to a final volume of 150 μ L and all the reaction components were incubated for 10 min at 37 °C prior to ATP addition. Samples were placed in a 96-well flat-bottom plate (Greiner Bio-One) and measurements of absorbance at 340 nm were done at 37 °C for 1 hour in an EnSpire 2300 Multilabel Reader (Perkin Elmer). Samples containing no proteins were used as controls for background NADH decomposition. ATP hydrolysis rates were calculated from the slope of the change in absorbance at 340 nm over time. All experiments were done at least in triplicate and standard deviations are presented.

End-point measurements in the presence of RPAP3, RPAP3-PIH1D1 and RPAP3 C-domain were performed using 5 mM ATP and RUVBL1/2 at 2 μ M hexamers; complexes were formed by mixing equimolar concentrations of RUVBL1 and RUVBL2, followed by incubation for at least 1 hour at 4 °C. Controls containing only RPAP3, RPAP3 C-domain and RPAP3-PIH1D1 were subtracted from their respective samples containing RUVBL1/2.

To obtain kinetic parameters of RUVBL1, RUVBL2, RUVBL1/2 ATPase activities, ATPase assays were performed using protein concentration of 10 μ M (monomers) and ATP concentrations varying from 0.1 mM to 7 mM. Michaelis-Menten constant (K_M), maximum velocity (V_{max}) and turnover number (k_{cat}) were calculated by fitting experimental initial velocity values of the proteins at different ATP concentrations using the equation:

$$V = \frac{V_{max}[S]}{K_M + [S]}$$

where V is the initial velocity, V_{max} is the maximum velocity, K_M is the Michaelis-Menten constant and $[S]$ is the molar concentration of the substrate.

Bioinformatics

Global sequence alignment was done using Clustal Omega (Madeira *et al.*, 2019). Sequence logos were constructed using the Weblogo 3 program (Crooks *et al.*, 2004). Protein secondary

structure and disorder were predicted by PSIPRED and DISOPRED servers (Buchan and Jones, 2019). The probability of coiled-coil formation was predicted by MARCOIL (Delorenzi and Speed, 2002) and hydropathy index was calculated using PONDR tool. Protein structure diagrams were generated using the PDBsum server (Laskowski *et al.*, 2018).

Spectroscopy experiments

Circular dichroism spectra were collected on a J-810 spectropolarimeter (Jasco) using full-length R2TP proteins at 0.10 mg/mL – 0.4 mg/mL in the buffer I. Data were collected from 198 to 260 nm, 0.5 nm data pitch, at scanning speed of 100 nm/min and response time of 0.5 sec. For RPAP3 ND, samples were used at 0.07 and 0.14 mg/mL and data were collected from 196 nm to 260 nm using the same spectropolarimeter setup. Thermal unfolding of RPAP3 ND was performed from 20°C to 80°C using 1°C/min heating rate, with acquisition of spectra every 20°C. All experiments were done using a 1 mm quartz cuvette. Protein spectra were subtracted from the blank and converted to mean residue ellipticity, $[\theta]$, using the equation:

$$[\theta] = \frac{\theta \times M \times 100}{n \times c \times l}$$

Where, θ is the circular dichroism signal in millidegrees, M is the molecular mass in kDa, n is the number of amino acid residues, c is the concentration in mg/mL and l is the pathlength in cm.

RPAP3 ND fluorescence emission spectra were acquired using a Fluorolog spectrofluorometer (HORIBA) with samples at 5 μ M, excitation wavelength at 280 nm and emission fluorescence collected from 300 nm to 450 nm, using 1 nm data pitch. Spectra from samples were subtracted from their respective blanks.

Analytical ultracentrifugation

Sedimentation velocity (SV-AUC) experiments were done with a ProteomeLab XL-A

analytical ultracentrifuge (Beckman) using the An60-Ti rotor. RPAP3 samples were prepared at 0.8 mg/mL in buffer I and data from 200 scans were collected at 20 °C, 25,000 rpm, using absorbance at 280 nm. Data analysis was performed using the Sedfit software (Schuck, 2000) with RPAP3 \bar{V} of 0.73591 cm³/g, and buffer density and viscosity of 1.0194 g/cm³ and 0.010556 P, respectively.

Small angle X-ray scattering (SAXS)

SAXS experiments were carried out at the SAXS1 beamline located at the Brazilian Synchrotron Light Laboratory (LNLS – CNPEM, Campinas, SP, Brazil). Scattering profiles were recorded using a 1.544 Å wavelength electron beam and a Pilatus 300K detector (Dectris), with a sample-to-detector distance of 898.39 mm, corresponding to the range $0.013 < q < 0.49$. RPAP3 and RPAP3-PIH1D1 samples were prepared in buffer L. RPAP3 samples were used at 0.6 mg/mL, 1 mg/mL, and 1.4 mg/mL; samples of RPAP3-PIH1D1 complex were used at 0.8 mg/mL, 1.8 mg/mL, and 2.6 mg/mL; RUVBL2 and RUVBL1/2 samples were prepared at 0.85 mg/mL (16.6 µM protomer for RUVBL2 and 16.8 µM protomer for RUVBL1/2) and 1.7 mg/mL (33.2 µM and 33.5 µM protomer for RUVBL2 and RUVBL1/2, respectively) in buffer E. To obtain protein scattering profiles, scattering curves of buffers were subtracted from their respective samples. All samples were collected at various time frames (10 sec to 300 sec) in order to inspect for X-ray damage. Standard deviations are shown for Guinier approximation analyses.

The ATSAS 2.7.2 package (Franke *et al.*, 2017) was used for SAXS data processing. Scattering curves were compared and merged into a single curve by PRIMUS and DATMERGE programs, respectively. The generation of pair distance distribution functions, $P(r)$, was done using the GNOM software (Svergun, 1992). *Ab initio* dummy atoms (DA) models were generated using a simulated-annealing methodology implemented in DAMMIN

and DAMMIF software (Franke and Svergun, 2009; Svergun, 1999). Using DAMMIF, twenty models were generated for each protein and P1 symmetry axis was imposed for RPAP3 and RPAP3-PIH1D1. Alignment, averaging and selection of the most probable DA models were done by the DAMAVER software package (Volkov and Svergun, 2003). DA model refinement was done by DAMMIN.

Ensemble optimization method was performed using the EOM 2.0 package (Tria *et al.*, 2015). Crystal structures of RPAP3 TPR1 (Pal *et al.*, 2014) and TPR2 (Henri *et al.*, 2018a) domains and C-domain (Maurizy *et al.*, 2018) were used in this approach. The high-resolution structures were connected by flexible linkers using $C\alpha$ distribution compatible to those from natively disordered structures. Ten thousand RPAP3 conformers were generated, and their respective size and dimension computed by the RANCH (Random Chains) program. The best ensemble of conformers describing the experimental RPAP3 scattering profile was selected by the genetic algorithm implemented in the GAJOE (Genetic Algorithm Judging Optimization of Ensembles) program. This selection was done 10 times and the curves represent the average of the results.

Rigid-body modeling simulations of complexes were done with the CORAL (Complexes with Random Loops) program (Petoukhov *et al.*, 2012). In the RUVBLs simulations, the crystal structures of RUVBL1 (Matias *et al.*, 2006) and RUVBL2 (Silva *et al.*, 2018a) were used. The regions of RUVBL1 comprising amino acid residues 1-42, 122-132, 202-239 and 450-456 were filled with dummy residues in order to obtain the full-length structure and to account for DII_{ext} flexibility. Similarly, amino acid residues from 1-48, 127-137, 212-243 and 457-463 were modeled by dummy residues in the RUVBL2 rigid-body models. RUVBL1 and RUVBL2 were positioned in the RUVBL1/2 heterodimer based on the crystal structure of RUVBL1/2 lacking their DII (Gorynia *et al.*, 2011). P6 symmetry axis was applied for RUVBL2, whereas P32 symmetry axis was used for RUVBL1/2. Generation of

rigid-body models was done 5 times for each protein complex and structures displaying the best fit to the experimental SAXS curves are shown. Centering of structures to the origin and alignment of PDB chains to coordinate axis were done by the ALPRAXIN software (Kozin and Svergun, 2001).

RPAP3-PIH1D1 rigid-body modelling was performed using a combination of CORAL and DAMCLUST (Petoukhov *et al.*, 2012) programs. Fifty RPAP3-PIH1D1 models were generated using RPAP3 crystal structures as described for EOM, and PIH1D1 PIH1 (Horejsi *et al.*, 2014) and CS (Henri *et al.*, 2018a) domains structures applying P1 symmetry axis. DAMCLUST was employed to cluster all 50 RPAP3-PIH1D1 models based on their normalized spatial discrepancy.

Mant-ADP fluorescence assays

Experiments with the fluorescent ADP analogue mant-ADP (Jena Bioscience) were performed using a Fluorolog spectrofluorometer (HORIBA). Samples were prepared in buffer Q as follows: (1) RUVBL1 = 1 μ M as hexamers, (2) RUVBL2 = 1 μ M as hexamers, (3) RUVBL1/2 = 1 μ M as heterohexamers, (4) R2TP = 1 μ M RUVBL1/2 as heterohexamers + 3 μ M RPAP3-PIH1D1 as heterodimers, (5) R2T = 1 μ M RUVBL1/2 as heterohexamers + 3 μ M RPAP3 as monomers, and (6) R2P = 1 μ M RUVBL1/2 as hexamers + 3 μ M PIH1D1 as monomers. Samples were incubated for 15 min on ice followed by 30 min with 6 μ M mant-ADP. Titration of ATP γ S and ADP were performed by adding increasing concentrations of the non-fluorescent nucleotides (0 to 60 μ M) to samples followed by incubation for at least 60 min on ice. Mant-ADP was excited at 355 nm (2 nm slit) and its fluorescence emission was collected from 400 nm to 600 nm (5 nm slit), using data pitch of 1 nm. Blank and control samples were submitted to the same procedures. Fluorescence spectra were analyzed by means of spectral center of mass $\langle\lambda\rangle$, using the equation:

$$\langle \lambda \rangle = \frac{\sum Fi \times \lambda i}{\sum Fi}$$

Where, Fi is the fluorescence intensity at each wavelength and λi is the wavelength.

Calculation of apparent dissociation constants (K_d^{app}) was done by fitting the normalized difference between initial and final $\langle \lambda \rangle$ ($\Delta \langle \lambda \rangle$) as function of ADP or ATP γ S concentration to a OneSiteBind function using Origin 7 software.

Mass photometry

Mass photometry measurements were performed as described in reference (Young *et al.*, 2018). Briefly, the output of a 520 nm laser diode (Lasertack) was collimated and sent through a pair of acousto-optic deflectors (AODs, AA Optoelectronic DTSXY-400). A 4f telecentric lens system imaged the deflection by the AODs into the back focal plane of the microscope objective (Olympus UApo N, 100x, 1.49 NA). The objective collected light reflected at the interface between a glass coverslip and some of the light scattered by the sample, with efficient separation of illumination and detection achieved through the combination of a polarizing beam splitter and quarter-wave plate (Thorlabs). The same telecentric lens system imaged the back focal plane of the objective onto a partial reflector made from a thin layer of silver of 2.5 mm diameter deposited onto a window, which selectively attenuates the reflected light compared to light from point scatters at the surface. A final lens imaged the sample onto a CMOS camera (Ximea, MC023MG-SY) with 277.8x magnification, resulting in a final pixel size of 21.1 nm/pixel. Borosilicate microscope coverslips (24x50 mm², #1.5H from Thorlabs, and 24x24 mm², No. 1.5 from VWR) used in these experiments were cleaned by ultra-sonication for 10 min in ultrapure water, followed by isopropanol and again ultrapure water, before being dried under a clean stream of nitrogen. Cleaned coverslips were assembled into flow chambers (Yildiz *et al.*, 2003). After introduction of ~15 μ L of sample to the flow chamber, images of a 3.5 x 12.2 μ m² region of the glass coverslip surface as proteins bind non-specifically from

solution were acquired at 1000 frames/s. The illuminating power density was 800 kW cm⁻². Prior to saving each movie file, areas of 4x4 pixels were binned for an effective pixel size of 84.4 nm/pixel, and frames were averaged 5-fold in time. Ratiometric frames were calculated, and mass distributions extracted as described previously (Cole et al., 2017; Young *et al.*, 2018). The contrast-to-mass conversion of the instrument was calibrated using the molecular weight standard proteins alcohol dehydrogenase and β -amylase, purchased from Sigma-Aldrich. Each protein was measured twice, and the measured contrasts of the dimer and tetramer peaks of each taken for calibration.

For the titration experiments, solutions of RUVBL1/2 at 0.2 μ M (heterohexamer concentration) were incubated on ice for ~30 mins together with the other component (RPAP3 iso1-PIH1D1, RPAP3 iso1, or PIH1D1) in concentrations of 0, 0.2, 0.4, 0.8 and 1.6 μ M. Solutions were diluted a further 10-fold immediately (<10 s) before adding to the flow chamber, to ensure sufficient separation in the images between the diffraction-limited features of single protein binding events. Two measurements were performed for each condition, and the data reported here are the combined results of the two. To characterize each component individually, the same procedure was carried for RPAP3-PIH1D1, RPAP3 and PIH1D1 at an incubation concentration of 0.4 μ M. The distribution shown for RUVBL1/2 was taken from 6 measurements of RUVBL1/2 without any other protein component present. Mass distributions were plotted as kernel density estimates (KDEs). A kernel bandwidth of 5 kDa was used to generate the KDEs for the individual protein components, while a bandwidth of 10 kDa was used for the titration experiments. In the latter case, the number of lower mass species can increase simply through the increasing concentration of the non-RUVBL1/2 component, potentially influencing the probability density estimate of the complexes containing at least one RUVBL1/2 unit even if no binding were to occur. To minimize this effect, therefore, only species of a mass greater than 240 kDa were considered in generating the KDE. The value of

240 kDa was chosen since it does not truncate the RUVBL1/2 peak around 300 kDa but does exclude most of the species arising from any of RPAP3, PIH1D1 or RPAP3-PIH1D1.

Nanoflow electron spray ionization mass spectrometry (NanoESI)

NanoESI mass spectrometry experiments were done in on a high mass Q-TOF-type instrument (Sobott *et al.*, 2002) adapted for a QSTAR CL platform (MDS Sciex) (Chernushevich and Thomson, 2004). Proteins samples were prepared in 100-500 mM ammonium acetate (pH 7.5) to a final concentration of 3.5-16 μ M, and 2 μ L of solutions were electrosprayed from gold-plated borosilicate glass capillaries made in-house as described elsewhere (Hernandez and Robinson, 2007). For mass spectrometry experiments, typical conditions employed capillary voltage at 1.3 kV, declustering potential of 90-100 V, focusing potential of 150 V, declustering potential two of 15 V, focusing rod offset varied from 60 to 100V, and MCP of 2550 V. External calibration was done by using a 100 mg/mL aqueous solution of cesium iodide (Sigma-Aldrich) (Park *et al.*, 2010).

Negative-stain electron microscopy

Untagged RUVBL1/2 samples were used at 0.05 mg/mL, and 10 μ L were applied to a carbon-plated grid previously glow-discharged and, subsequently, negatively stained with 0.8% (w/v) uranyl formate or 1% (w/v) uranyl acetate. Samples were imaged in a JEOL 2010F transmission electron microscope operated at 200 kV. Images were collected at 50,000x magnification with an electron dose of 10 $e^-/\text{\AA}^2$, recorded on SO-163 films (Kodak), scanned on a Super COOLSCAN 9000 ED (Nikon) at 6.35 μ m/pixel and averaged 2x to produce data at 2.54 \AA /pixel. Particles were extracted interactively from digitalized fields using the “Boxer” program (EMAN) (Ludtke *et al.*, 1999). For eXact tag RUVBL1/2 complexes, proteins were expressed and purified as previously reported by our group (Nano *et al.*, 2020). Briefly,

bacterial cells transformed with the plasmid for co-expression of RUVBL1-H₆ and eXact tag-RUVBL2 (Table S5) were grown at 37 °C until OD₆₀₀ = 0.6. The temperature was then decreased to 18 °C and protein expression was induced overnight by 1 mM IPTG. Cells were harvested by centrifugation at 3,000 x g for 10 minutes, resuspended in buffer A and disrupted by sonication on ice. The lysate was spun down at 12,000 x g for 30 min at 4 °C, the supernatant collected and submitted to IMAC, His-tag removal and ion exchange chromatography as described in the second and third paragraphs of the “Protein expression and purification” section of Method Details. Negative staining was done by deposition of eXact tag RUVBL1/2 on a glow-discharged carbon-coated copper grid, followed by washing with two drops of ultrapure water and staining with two drops of 0.75% (w/v) uranyl formate (Ohi et al., 2004). Images were collected in a T12 (FEI) at 1-2 mm defocus and recorded using a 4k CCD camera (Gatan) (Ewens et al., 2016).

Cross-linking followed by mass spectrometry (XL-MS)

Cross-linking of human R2TP was done with 4.4 μM of the complex consisting of one RUVBL1/2 hexamer bound to three RPAP3-PIH1D1 in buffer M. Proteins were crosslinked with a 250-fold molar excess MS-cleavable membrane-permeable crosslinker, disuccinimidyl sulfoxide (DSSO, Thermo Scientific). Briefly, proteins were reduced with 10 mM (DTT), alkylated with 50 mM iodoacetamide, denatured with 2 M Urea and 0.01 % ProteaseMAX surfactant (Promega) and digested with Trypsin Gold 1:20 (w/w) (Promega) at 37 °C for two hours. Peptides were desalted using C-18 packed TopTip (Glygen) and dried using a SpeedVac Concentrator (SVC 100H, Savant). After resuspension in 10% formic acid, peptides were subjected to strong cation exchange chromatography in a Luna SCX column (50 x 2 mm, 5 μm, 100 Å, Phenomenex) connected to an Agilent 1100 HPLC system following the method previously described (Liu et al., 2015). Fractions (96 in total) were compiled into 5 pools based

on the elution profile. Peptides were desalted using C-18 packed TopTip (Glygen) and dried.

After 100-fold dilution, 5 μ L of the DSSO cross-linked peptides were separated by reverse phase chromatography using an EASY-nLC 1000 (Thermo Fisher Scientific) with an in-house prepared reverse phase nano-analytical column Reprosil-Pur 120 C-18-AQ (75 μ m I.D., 25 cm length, 3 μ m, 120 Å, Dr. Maisch GmbH), at a flow rate of 400 nL/min. The chromatography system was coupled to an Orbitrap Fusion Tribrid mass spectrometer (Thermo Fisher Scientific) equipped with a Nanospray Flex NG source (Thermo Fisher Scientific). The Orbitrap Fusion 3.0 instrument parameters were as follows for the Orbitrap (OT-MS) with MS2 OT-CID and DSSO mass doublet triggered MS3 IT-CID analysis: Nano-electrospray ion source with spray voltage 2.55 kV, capillary temperature 275 °C. Survey MS1 scan m/z range 400-1800 profile mode, resolution 60,000 FWHM@200m/z one microscan with maximum inject time 50 msec. Data-dependent acquisition Orbitrap survey spectra were scheduled at least every 5 sec, with the software determining 'Top-speed' number of MS/MS acquisitions during this period. The automatic gain control (AGC) target values for FTMS and MSn were 400,000 and 50,000 (MS2) and 10,000 (MS3) respectively. The most intense ions charge state 4-10 exceeding 50,000 counts were selected for CID MSMS fragmentation with orbitrap detection in centroid mode. Monoisotopic Precursor Selection (MIPS) was enabled, and Dynamic exclusion settings were as follows: repeat count 1; exclusion duration 18 sec with a 5 ppm mass window. The ddMS2 OT CID scan used a quadrupole isolation window of 1.6 Da; 15,000 Orbitrap resolution normal scan range, centroid detection, first mass 120 m/z, 1 microscan, 120 msec maximum injection time and normalized collision energy setting 25%. When a mass difference of 31.9721 m/z corresponding to a DSSO crosslink signature was observed in the CID-MS2 scan, an additional ddMS³ IT CID was triggered on both ions for the top 4 most intense signals, charge state 2-6 using an MS isolation window 2 m/z, MS2 isolation window 2 m/z, IonTrap rapid scan rate centroid detection, 1 microscan, 100 msec maximum

injection time, CID activation time 10 msec injection time, AGC target 10,000 and collision energy 30%.

Raw files were created by XCalibur 4.1.31.9 (Thermo Fisher Scientific) software and analyzed with the Proteome Discoverer software suite 2.2 (Thermo Fisher Scientific) with incorporated XlinkX nodes. Spectra were matched against the *H. sapiens* database from SwissProt (version 2018_06, 20 349 sequences, downloaded from UniProt). The protease was set to 'Trypsin', and the maximum number of missed cleavages was defined as 2. Carbamidomethylation of cysteines was set as a fixed modification and oxidation of methionine as variable modification. For the linear peptide search, precursor mass tolerance was defined as 10 ppm, and fragment mass tolerance was defined as 0.6 Da. Cross-linked peptides were matched against a protein sequence database of RT2P complex subunits, with crosslink modification set to DSSO/ +158.004 Da (K), the minimum peptide length to 5, minimum peptide mass to 300, and the maximum peptide mass to 7000. The precursor mass tolerance was set to 10 ppm, FTMS fragment mass tolerance was set at 20 ppm and ITMS fragment mass was set at 0.5 Da. FDR threshold was set to 0.01 (1%), and FDR strategy was set as 'Percolator'. Visualization of cross-linked peptides was done using the xiVIEW tool (Graham *et al.*, 2019).

Affinity purification followed by mass spectrometry (AP-MS)

HEK293T extracts were produced by lysing cells using buffer O, followed by sonication. After removal of cellular debris by centrifugation (10,000 x g, 10 min, 4°C), cell lysates were incubated for 30 min on ice with recombinant purified His₁₂-SUMO-RPAP3 ND previously immobilized on HisPur Co²⁺ beads (Thermo Fisher Scientific). Control experiments were performed incubating cell extracts with immobilized His₁₂-SUMO on Co²⁺ beads. Beads were washed four times with buffer P and elution of His₁₂-SUMO-RPAP3 ND-interacting proteins

was performed using Ulp1 protease. All control samples were submitted to the same treatment. Mass spectrometry analysis was performed based on previously described (Wu et al., 2019). Samples were reduced with 5 mM TCEP for 30 min, alkylated with 15 mM iodoacetamide for 30 min in the dark, followed by denaturation with 2M Urea and subsequent digestion by overnight incubation with Trypsin Gold 1:20 (w/w) (Promega) at 37 °C. C18 packed TopTip (Glygen) was used to desalt tryptic peptides, that were subsequently dried in a SpeedVac vacuum concentrator (SVC 100H, Savant) and resuspended in 0.1% (v/v) formic acid. Peptides were separated by chromatography using an in-house packed nano C18 column (10 cm x 75 µm ID, 3 µm, 100 Å) connected to a Proxeon EASY-nCL 1000 (Thermo Fisher Scientific). A water/acetonitrile/0.1% (v/v) formic acid 100 min gradient at flow rate of 300 nL/min, consisting of 1% to 3% acetonitrile increase in the first 2 min, followed by a linear gradient from 3% to 24% acetonitrile for 74 min, a linear gradient from 24% to 100% for 14 min, and a 10 min wash with 100% acetonitrile, was employed. Eluted peptides were directly sprayed into the Orbitrap Elite Mass Spectrometer (Thermo Fisher Scientific) by positive electrospray ionization at an ion source temperature of 250 °C and ion spray voltage of 2.1 kV. Full-scan mass spectrometry spectra (m/z 350-2,000) were collected in the Orbitrap at 60,000 (m/z 400) resolution. Automatic gain control was set to 1e6 for full FTMS scans and 5e4 for MS/MS scans. The 15 most intense ions with charge state ≥ 2 were isolated and fragmented in the linear ion trap by low-energy CID. Ions intensity exceeding 1,500 counts were submitted to CID with normalized collision energy set at 35%, activation Q at 0.250 and an activation time of 10 ms. MS raw files were converted into mzXML format and identification of peptides was performed using SEQUEST (Eng *et al.*, 1994) against human proteins sequences. Only identified peptides with probability higher than 80% were used for further analysis. Filtering of identified proteins was performed using CRAPome server (Mellacheruvu *et al.*, 2013). DAVID server (Huang *et al.*, 2009b) was used for functional enrichment analysis and InteractiVenn (Heberle *et al.*,

2015) was employed for generation of Venn diagrams.

QUANTIFICATION AND STATISTICAL ANALYSIS

Statistical analyses are described in figures and tables. Data in Table S1 represents mean \pm SD for each experiment calculated by ASTRA 7.1 software. In Table S2, Guinier data represents mean \pm SD calculated by PRIMUS software for individual merged curves. In Figure 3F and Table S2, EOM data for RPAP3 are described as mean \pm SD from 10 simulations calculated in Origin 7 software. In Table S2, RPAP3-PIH1D1 CORAL data represents mean \pm SD from the 7 representative models calculated using Origin 7 software. In Figure 7A,B,C and Figure S3F, values representing mean \pm SD were calculated in Origin 7 software from at least 3 experiments. Data in Figure 7D are described as box charts, where interquartile range (large box), mean (small box), median (horizontal line), 5th and 95th percentile (whiskers) and maximum and minimum values (asterisks), were calculated in Origin 7 software from at least 3 experiments. Statistical *p*-values in Figure 8 and Table S3 were determined by a modified Fisher Exact *p*-value, EASE score, by DAVID server.

REFERENCES

- Andersen, K.R., Leksa, N.C., and Schwartz, T.U. (2013). Optimized E. coli expression strain LOBSTR eliminates common contaminants from His-tag purification. *Proteins* 81, 1857-1861. 10.1002/prot.24364.
- Aramayo, R.J., Willhoft, O., Ayala, R., Bythell-Douglas, R., Wigley, D.B., and Zhang, X. (2018). Cryo-EM structures of the human INO80 chromatin-remodeling complex. *Nat Struct Mol Biol* 25, 37-44. 10.1038/s41594-017-0003-7.
- Boulon, S., Pradet-Balade, B., Verheggen, C., Molle, D., Boireau, S., Georgieva, M., Azzag, K., Robert, M.C., Ahmad, Y., Neel, H., et al. (2010). HSP90 and its R2TP/Prefoldin-like cochaperone are involved in the cytoplasmic assembly of RNA polymerase II. *Mol. Cell* 39, 912-924. 10.1016/j.molcel.2010.08.023.
- Buchan, D.W.A., and Jones, D.T. (2019). The PSIPRED Protein Analysis Workbench: 20 years on. *Nucleic Acids Res.* 47, W402-w407. 10.1093/nar/gkz297.
- Chemes, L.B., Alonso, L.G., Noval, M.G., and de Prat-Gay, G. (2012). Circular dichroism techniques for the analysis of intrinsically disordered proteins and domains. *Methods Mol. Biol.* 895, 387-404. 10.1007/978-1-61779-927-3_22.
- Chernushevich, I.V., and Thomson, B.A. (2004). Collisional cooling of large ions in electrospray mass spectrometry. *Anal. Chem.* 76, 1754-1760. 10.1021/ac035406j.
- Cheung, K.L., Huen, J., Kakihara, Y., Houry, W.A., and Ortega, J. (2010). Alternative oligomeric states of the yeast Rvb1/Rvb2 complex induced by histidine tags. *J. Mol. Biol.* 404, 478-492. 10.1016/j.jmb.2010.10.003.
- Cloutier, P., Poitras, C., Durand, M., Hekmat, O., Fiola-Masson, E., Bouchard, A., Faubert, D., Chabot, B., and Coulombe, B. (2017). R2TP/Prefoldin-like component RUVBL1/RUVBL2 directly interacts with ZNHIT2 to regulate assembly of U5 small nuclear ribonucleoprotein. *Nat Commun* 8, 15615. 10.1038/ncomms15615.
- Cole, D., Young, G., Weigel, A., Sebesta, A., and Kukura, P. (2017). Label-Free Single-Molecule Imaging with Numerical-Aperture-Shaped Interferometric Scattering Microscopy. *ACS Photonics* 4, 211-216. 10.1021/acsp Photonics.6b00912.
- Crooks, G.E., Hon, G., Chandonia, J.M., and Brenner, S.E. (2004). WebLogo: a sequence logo generator. *Genome Res.* 14, 1188-1190. 10.1101/gr.849004.
- Delorenzi, M., and Speed, T. (2002). An HMM model for coiled-coil domains and a comparison with PSSM-based predictions. *Bioinformatics* 18, 617-625. 10.1093/bioinformatics/18.4.617.
- Eng, J.K., McCormack, A.L., and Yates, J.R. (1994). An approach to correlate tandem mass spectral data of peptides with amino acid sequences in a protein database. *J. Am. Soc. Mass Spectrom.* 5, 976-989. 10.1016/1044-0305(94)80016-2.
- Ewens, C.A., Su, M., Zhao, L., Nano, N., Houry, W.A., and Southworth, D.R. (2016). Architecture and Nucleotide-Dependent Conformational Changes of the Rvb1-Rvb2 AAA+

Complex Revealed by Cryoelectron Microscopy. *Structure* 24, 657-666. 10.1016/j.str.2016.03.018.

Franke, D., Petoukhov, M.V., Konarev, P.V., Panjkovich, A., Tuukkanen, A., Mertens, H.D.T., Kikhney, A.G., Hajizadeh, N.R., Franklin, J.M., Jeffries, C.M., and Svergun, D.I. (2017). ATSAS 2.8: a comprehensive data analysis suite for small-angle scattering from macromolecular solutions. *J Appl Crystallogr* 50, 1212-1225. 10.1107/S1600576717007786.

Franke, D., and Svergun, D.I. (2009). DAMMIF, a program for rapid ab-initio shape determination in small-angle scattering. *J Appl Crystallogr* 42, 342-346. 10.1107/S0021889809000338.

Gorynia, S., Bandejas, T.M., Pinho, F.G., McVey, C.E., Vonrhein, C., Round, A., Svergun, D.I., Donner, P., Matias, P.M., and Carrondo, M.A. (2011). Structural and functional insights into a dodecameric molecular machine - the RuvBL1/RuvBL2 complex. *J. Struct. Biol.* 176, 279-291. 10.1016/j.jsb.2011.09.001.

Graham, M., Combe, C., Kolbowski, L., and Rappsilber, J. (2019). xiView: A common platform for the downstream analysis of Crosslinking Mass Spectrometry data. *bioRxiv*, 561829. 10.1101/561829.

Heberle, H., Meirelles, G.V., da Silva, F.R., Telles, G.P., and Minghim, R. (2015). InteractiVenn: a web-based tool for the analysis of sets through Venn diagrams. *BMC Bioinformatics* 16, 169. 10.1186/s12859-015-0611-3.

Henri, J., Chagot, M.E., Bourguet, M., Abel, Y., Terral, G., Maurizy, C., Aigueperse, C., Georgescauld, F., Vandermoere, F., Saint-Fort, R., et al. (2018a). Deep Structural Analysis of RPAP3 and PIH1D1, Two Components of the HSP90 Co-chaperone R2TP Complex. *Structure* 26, 1196-1209 e1198. 10.1016/j.str.2018.06.002.

Henri, J., Chagot, M.E., Bourguet, M., Abel, Y., Terral, G., Maurizy, C., Aigueperse, C., Georgescauld, F., Vandermoere, F., Saint-Fort, R., et al. (2018b). Deep Structural Analysis of RPAP3 and PIH1D1, Two Components of the HSP90 Co-chaperone R2TP Complex. *Structure* 26, 1196-1209.e1198. 10.1016/j.str.2018.06.002.

Hernandez, H., and Robinson, C.V. (2007). Determining the stoichiometry and interactions of macromolecular assemblies from mass spectrometry. *Nat. Protoc.* 2, 715-726. 10.1038/nprot.2007.73.

Horejsi, Z., Stach, L., Flower, T.G., Joshi, D., Flynn, H., Skehel, J.M., O'Reilly, N.J., Ogrodowicz, R.W., Smerdon, S.J., and Boulton, S.J. (2014). Phosphorylation-dependent PIH1D1 interactions define substrate specificity of the R2TP cochaperone complex. *Cell reports* 7, 19-26. 10.1016/j.celrep.2014.03.013.

Horejsi, Z., Takai, H., Adelman, C.A., Collis, S.J., Flynn, H., Maslen, S., Skehel, J.M., de Lange, T., and Boulton, S.J. (2010). CK2 phospho-dependent binding of R2TP complex to TEL2 is essential for mTOR and SMG1 stability. *Mol. Cell* 39, 839-850. 10.1016/j.molcel.2010.08.037.

Houry, W.A., Bertrand, E., and Coulombe, B. (2018). The PAQosome, an R2TP-Based Chaperone for Quaternary Structure Formation. *Trends Biochem. Sci.* 43, 4-9. 10.1016/j.tibs.2017.11.001.

- Huang da, W., Sherman, B.T., and Lempicki, R.A. (2009a). Bioinformatics enrichment tools: paths toward the comprehensive functional analysis of large gene lists. *Nucleic Acids Res.* 37, 1-13. 10.1093/nar/gkn923.
- Huang da, W., Sherman, B.T., and Lempicki, R.A. (2009b). Systematic and integrative analysis of large gene lists using DAVID bioinformatics resources. *Nat. Protoc.* 4, 44-57. 10.1038/nprot.2008.211.
- James, P., Halladay, J., and Craig, E.A. (1996). Genomic libraries and a host strain designed for highly efficient two-hybrid selection in yeast. *Genetics* 144, 1425-1436.
- Kamano, Y., Saeki, M., Egusa, H., Kakiyama, Y., Houry, W.A., Yatani, H., and Kamisaki, Y. (2013). PIH1D1 interacts with mTOR complex 1 and enhances ribosome RNA transcription. *FEBS Lett.* 587, 3303-3308. 10.1016/j.febslet.2013.09.001.
- Kikhney, A.G., and Svergun, D.I. (2015). A practical guide to small angle X-ray scattering (SAXS) of flexible and intrinsically disordered proteins. *FEBS Lett.* 589, 2570-2577. 10.1016/j.febslet.2015.08.027.
- Kozin, M.B., and Svergun, D.I. (2001). Automated matching of high- and low-resolution structural models. *Journal of Applied Crystallography* 34, 33-41. 10.1107/s0021889800014126.
- Lakomek, K., Stoeck, G., Tosi, A., Schmailzl, M., and Hopfner, K.P. (2015). Structural basis for dodecameric assembly states and conformational plasticity of the full-length AAA+ ATPases Rvb1 . Rvb2. *Structure* 23, 483-495. 10.1016/j.str.2014.12.015.
- Laskowski, R.A., Jabłońska, J., Pravda, L., Vařeková, R.S., and Thornton, J.M. (2018). PDBsum: Structural summaries of PDB entries. *Protein Sci.* 27, 129-134. 10.1002/pro.3289.
- Lee, C.D., Sun, H.C., Hu, S.M., Chiu, C.F., Homhuan, A., Liang, S.M., Leng, C.H., and Wang, T.F. (2008). An improved SUMO fusion protein system for effective production of native proteins. *Protein Sci.* 17, 1241-1248. 10.1110/ps.035188.108.
- Liu, F., Rijkers, D.T., Post, H., and Heck, A.J. (2015). Proteome-wide profiling of protein assemblies by cross-linking mass spectrometry. *Nature methods* 12, 1179-1184. 10.1038/nmeth.3603.
- Lopez-Perrote, A., Munoz-Hernandez, H., Gil, D., and Llorca, O. (2012). Conformational transitions regulate the exposure of a DNA-binding domain in the RuvBL1-RuvBL2 complex. *Nucleic Acids Res.* 40, 11086-11099. 10.1093/nar/gks871.
- Ludtke, S.J., Baldwin, P.R., and Chiu, W. (1999). EMAN: semiautomated software for high-resolution single-particle reconstructions. *J. Struct. Biol.* 128, 82-97. 10.1006/jsbi.1999.4174.
- Machado-Pinilla, R., Liger, D., Leulliot, N., and Meier, U.T. (2012). Mechanism of the AAA+ ATPases pontin and reptin in the biogenesis of H/ACA RNPs. *RNA* 18, 1833-1845. 10.1261/rna.034942.112.
- Madeira, F., Park, Y.M., Lee, J., Buso, N., Gur, T., Madhusoodanan, N., Basutkar, P., Tivey, A.R.N., Potter, S.C., Finn, R.D., and Lopez, R. (2019). The EMBL-EBI search and sequence analysis tools APIs in 2019. *Nucleic Acids Res.* 47, W636-w641. 10.1093/nar/gkz268.

- Malinova, A., Cvackova, Z., Mateju, D., Horejsi, Z., Abeza, C., Vandermoere, F., Bertrand, E., Stanek, D., and Verheggen, C. (2017). Assembly of the U5 snRNP component PRPF8 is controlled by the HSP90/R2TP chaperones. *J. Cell Biol.* 216, 1579-1596. 10.1083/jcb.201701165.
- Martino, F., Pal, M., Munoz-Hernandez, H., Rodriguez, C.F., Nunez-Ramirez, R., Gil-Carton, D., Degliesposti, G., Skehel, J.M., Roe, S.M., Prodromou, C., et al. (2018). RPAP3 provides a flexible scaffold for coupling HSP90 to the human R2TP co-chaperone complex. *Nat Commun* 9, 1501. 10.1038/s41467-018-03942-1.
- Matias, P.M., Gorynia, S., Donner, P., and Carrondo, M.A. (2006). Crystal structure of the human AAA+ protein RuvBL1. *J Biol Chem* 281, 38918-38929. 10.1074/jbc.M605625200.
- Maurizy, C., Quinternet, M., Abel, Y., Verheggen, C., Santo, P.E., Bourguet, M., A, C.F.P., Bragantini, B., Chagot, M.E., Robert, M.C., et al. (2018). The RPAP3-Cterminal domain identifies R2TP-like quaternary chaperones. *Nat Commun* 9, 2093. 10.1038/s41467-018-04431-1.
- Mellacheruvu, D., Wright, Z., Couzens, A.L., Lambert, J.P., St-Denis, N.A., Li, T., Miteva, Y.V., Hauri, S., Sardi, M.E., Low, T.Y., et al. (2013). The CRAPome: a contaminant repository for affinity purification-mass spectrometry data. *Nature methods* 10, 730-736. 10.1038/nmeth.2557.
- Mir, R.A., Bele, A., Mirza, S., Srivastava, S., Olou, A.A., Ammons, S.A., Kim, J.H., Gurumurthy, C.B., Qiu, F., Band, H., and Band, V. (2015). A Novel Interaction of Ecdysoneless (ECD) Protein with R2TP Complex Component RUVBL1 Is Required for the Functional Role of ECD in Cell Cycle Progression. *Mol. Cell. Biol.* 36, 886-899. 10.1128/MCB.00594-15.
- Munoz-Hernandez, H., Pal, M., Rodriguez, C.F., Fernandez-Leiro, R., Prodromou, C., Pearl, L.H., and Llorca, O. (2019). Structural mechanism for regulation of the AAA-ATPases RUVBL1-RUVBL2 in the R2TP co-chaperone revealed by cryo-EM. *Sci Adv* 5, eaaw1616. 10.1126/sciadv.aaw1616.
- Nano, N., Ugwu, F., Seraphim, T.V., Li, T., Azer, G., Isaac, M., Prakesch, M., Barbosa, L.R.S., Ramos, C.H.I., Datti, A., and Houry, W.A. (2020). Sorafenib as an Inhibitor of RUVBL2. *Biomolecules* 10. 10.3390/biom10040605.
- Norby, J.G. (1988). Coupled assay of Na⁺,K⁺-ATPase activity. *Methods Enzymol.* 156, 116-119. 10.1016/0076-6879(88)56014-7.
- Ohi, M., Li, Y., Cheng, Y., and Walz, T. (2004). Negative Staining and Image Classification - Powerful Tools in Modern Electron Microscopy. *Biol. Proced. Online* 6, 23-34. 10.1251/bpo70.
- Pal, M., Morgan, M., Phelps, S.E., Roe, S.M., Parry-Morris, S., Downs, J.A., Polier, S., Pearl, L.H., and Prodromou, C. (2014). Structural basis for phosphorylation-dependent recruitment of Tel2 to Hsp90 by Pih1. *Structure* 22, 805-818. 10.1016/j.str.2014.04.001.
- Pal, M., Muñoz-Hernandez, H., Bjorklund, D., Zhou, L., Degliesposti, G., Skehel, J.M., Hesketh, E.L., Thompson, R.F., Pearl, L.H., Llorca, O., and Prodromou, C. (2021). Structure

of the TELO2-TTI1-TTI2 complex and its function in TOR recruitment to the R2TP chaperone. *Cell reports* 36, 109317. 10.1016/j.celrep.2021.109317.

Park, A.Y., Jergic, S., Politis, A., Ruotolo, B.T., Hirshberg, D., Jessop, L.L., Beck, J.L., Barsky, D., O'Donnell, M., Dixon, N.E., and Robinson, C.V. (2010). A single subunit directs the assembly of the *Escherichia coli* DNA sliding clamp loader. *Structure* 18, 285-292. 10.1016/j.str.2010.01.009.

Petoukhov, M.V., Franke, D., Shkumatov, A.V., Tria, G., Kikhney, A.G., Gajda, M., Gorba, C., Mertens, H.D., Konarev, P.V., and Svergun, D.I. (2012). New developments in the ATSAS program package for small-angle scattering data analysis. *J Appl Crystallogr* 45, 342-350. 10.1107/S0021889812007662.

Pettersen, E.F., Goddard, T.D., Huang, C.C., Meng, E.C., Couch, G.S., Croll, T.I., Morris, J.H., and Ferrin, T.E. (2021). UCSF ChimeraX: Structure visualization for researchers, educators, and developers. *Protein Sci.* 30, 70-82. 10.1002/pro.3943.

Petukhov, M., Dagkessamanskaja, A., Bommer, M., Barrett, T., Tsaneva, I., Yakimov, A., Queval, R., Shvetsov, A., Khodorkovskiy, M., Kas, E., and Grigoriev, M. (2012). Large-scale conformational flexibility determines the properties of AAA+ TIP49 ATPases. *Structure* 20, 1321-1331. 10.1016/j.str.2012.05.012.

Rivera-Calzada, A., Pal, M., Munoz-Hernandez, H., Luque-Ortega, J.R., Gil-Carton, D., Degliesposti, G., Skehel, J.M., Prodromou, C., Pearl, L.H., and Llorca, O. (2017). The Structure of the R2TP Complex Defines a Platform for Recruiting Diverse Client Proteins to the HSP90 Molecular Chaperone System. *Structure* 25, 1145-1152 e1144. 10.1016/j.str.2017.05.016.

Scheich, C., Kummel, D., Soumailakakis, D., Heinemann, U., and Bussow, K. (2007). Vectors for co-expression of an unrestricted number of proteins. *Nucleic Acids Res.* 35, e43. 10.1093/nar/gkm067.

Schuck, P. (2000). Size-distribution analysis of macromolecules by sedimentation velocity ultracentrifugation and lamm equation modeling. *Biophys. J.* 78, 1606-1619. 10.1016/S0006-3495(00)76713-0.

Seraphim, T.V., and Houry, W.A. (2020). AAA+ proteins. *Curr. Biol.* 30, R251-R257. 10.1016/j.cub.2020.01.044.

Silva, S.T.N., Brito, J.A., Arranz, R., Sorzano, C.O.S., Ebel, C., Douth, J., Tully, M.D., Carazo, J.M., Carrascosa, J.L., Matias, P.M., and Bandejas, T.M. (2018a). X-ray structure of full-length human RuvB-Like 2 - mechanistic insights into coupling between ATP binding and mechanical action. *Sci. Rep.* 8, 13726. 10.1038/s41598-018-31997-z.

Silva, S.T.N., Brito, J.A., Arranz, R., Sorzano, C.S., Ebel, C., Douth, J., Tully, M.D., Carazo, J.M., Carrascosa, J.L., Matias, P.M., and Bandejas, T.M. (2018b). X-ray structure of full-length human RuvB-Like 2 - mechanistic insights into coupling between ATP binding and mechanical action. *Sci Rep* 8, 13726. 10.1038/s41598-018-31997-z.

Silva-Martin, N., Daudén, M.I., Glatt, S., Hoffmann, N.A., Kastiris, P., Bork, P., Beck, M., and Müller, C.W. (2016). The Combination of X-Ray Crystallography and Cryo-Electron

Microscopy Provides Insight into the Overall Architecture of the Dodecameric Rvb1/Rvb2 Complex. *PLoS One* 11, e0146457. 10.1371/journal.pone.0146457.

Sobott, F., Hernandez, H., McCammon, M.G., Tito, M.A., and Robinson, C.V. (2002). A tandem mass spectrometer for improved transmission and analysis of large macromolecular assemblies. *Anal. Chem.* 74, 1402-1407. 10.1021/ac0110552.

Svergun, D. (1992). Determination of the regularization parameter in indirect-transform methods using perceptual criteria. *Journal of Applied Crystallography* 25, 495-503. doi:10.1107/S0021889892001663 %U <https://doi.org/10.1107/S0021889892001663>.

Svergun, D.I. (1999). Restoring low resolution structure of biological macromolecules from solution scattering using simulated annealing. *Biophys. J.* 76, 2879-2886. 10.1016/S0006-3495(99)77443-6.

Tria, G., Mertens, H.D., Kachala, M., and Svergun, D.I. (2015). Advanced ensemble modelling of flexible macromolecules using X-ray solution scattering. *IUCrJ* 2, 207-217. 10.1107/S205225251500202X.

Volkov, V.V., and Svergun, D.I. (2003). Uniqueness of ab initio shape determination in small-angle scattering. *Journal of Applied Crystallography* 36, 860-864. doi:10.1107/S0021889803000268 %U <https://doi.org/10.1107/S0021889803000268>.

von Morgen, P., Burdova, K., Flower, T.G., O'Reilly, N.J., Boulton, S.J., Smerdon, S.J., Macurek, L., and Horejsi, Z. (2017). MRE11 stability is regulated by CK2-dependent interaction with R2TP complex. *Oncogene* 36, 4943-4950. 10.1038/onc.2017.99.

Wu, Z., Malty, R., Moutaoufik, M.T., Zhang, Q., Jessulat, M., and Babu, M. (2019). A Tag-Based Affinity Purification Mass Spectrometry Workflow for Systematic Isolation of the Human Mitochondrial Protein Complexes. *Adv. Exp. Med. Biol.* 1158, 83-100. 10.1007/978-981-13-8367-0_6.

Yildiz, A., Forkey, J.N., McKinney, S.A., Ha, T., Goldman, Y.E., and Selvin, P.R. (2003). Myosin V walks hand-over-hand: single fluorophore imaging with 1.5-nm localization. *Science* 300, 2061-2065. 10.1126/science.1084398.

Yoshida, M., Saeki, M., Egusa, H., Irie, Y., Kamano, Y., Uruguchi, S., Sotozono, M., Niwa, H., and Kamisaki, Y. (2013). RPAP3 splicing variant isoform 1 interacts with PIH1D1 to compose R2TP complex for cell survival. *Biochem. Biophys. Res. Commun.* 430, 320-324. 10.1016/j.bbrc.2012.11.017.

Young, G., Hundt, N., Cole, D., Fineberg, A., Andrecka, J., Tyler, A., Olerinyova, A., Ansari, A., Marklund, E.G., Collier, M.P., et al. (2018). Quantitative mass imaging of single biological macromolecules. *Science* 360, 423-427. 10.1126/science.aar5839.

Zhao, R., Davey, M., Hsu, Y.C., Kaplanek, P., Tong, A., Parsons, A.B., Krogan, N., Cagney, G., Mai, D., Greenblatt, J., et al. (2005). Navigating the chaperone network: an integrative map of physical and genetic interactions mediated by the hsp90 chaperone. *Cell* 120, 715-727. 10.1016/j.cell.2004.12.024.

Zur Lage, P., Stefanopoulou, P., Styczynska-Soczka, K., Quinn, N., Mali, G., von Kriegsheim, A., Mill, P., and Jarman, A.P. (2018). Ciliary dynein motor preassembly is regulated by Wdr92

in association with HSP90 co-chaperone, R2TP. *J. Cell Biol.* 217, 2583-2598.
10.1083/jcb.201709026.

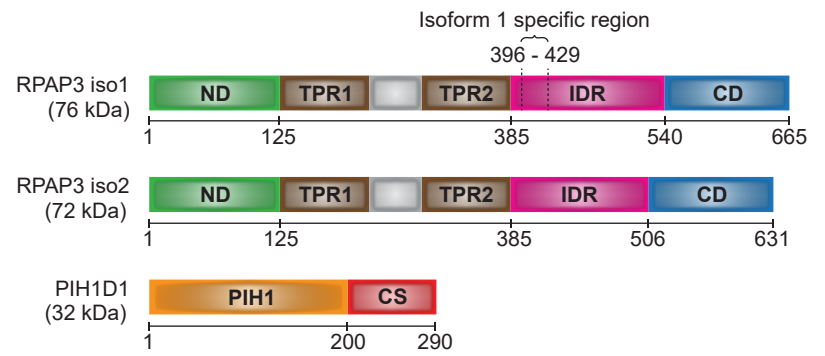
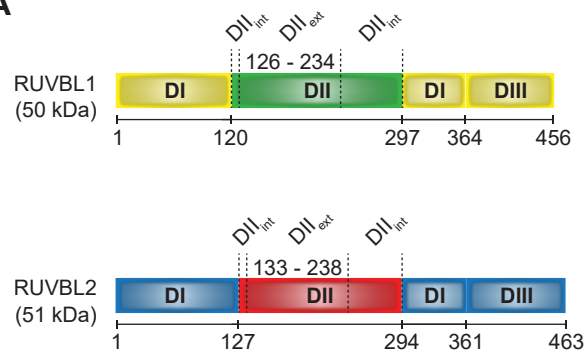
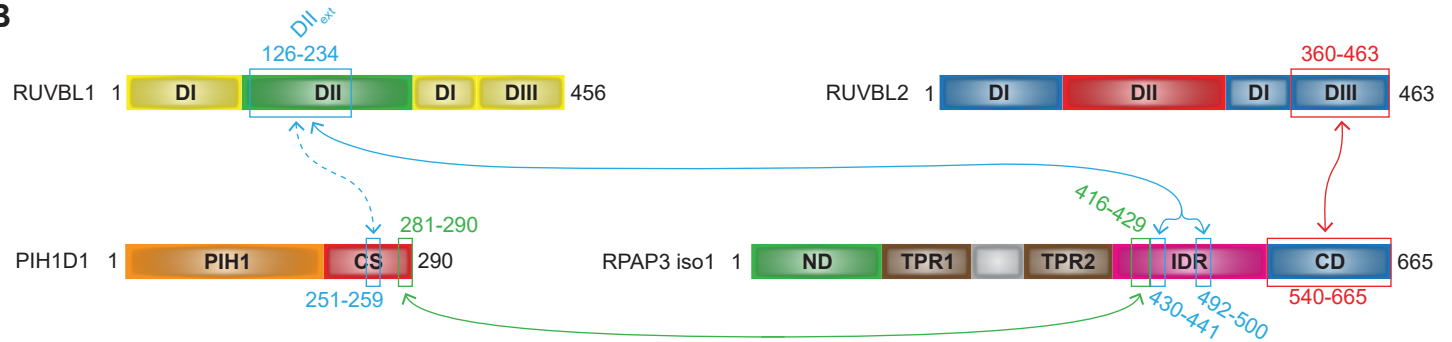
A**B**

Figure 1

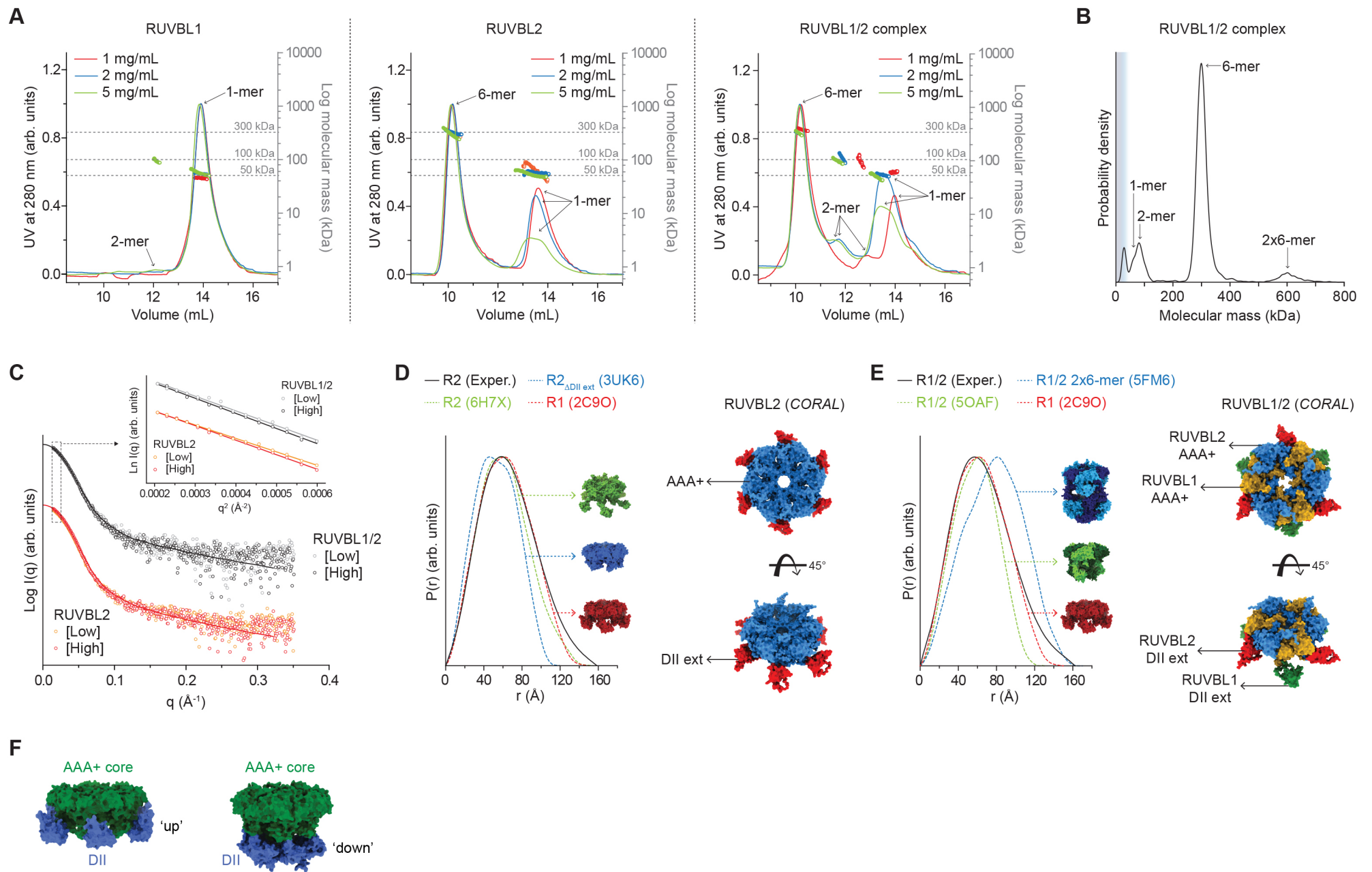


Figure 2

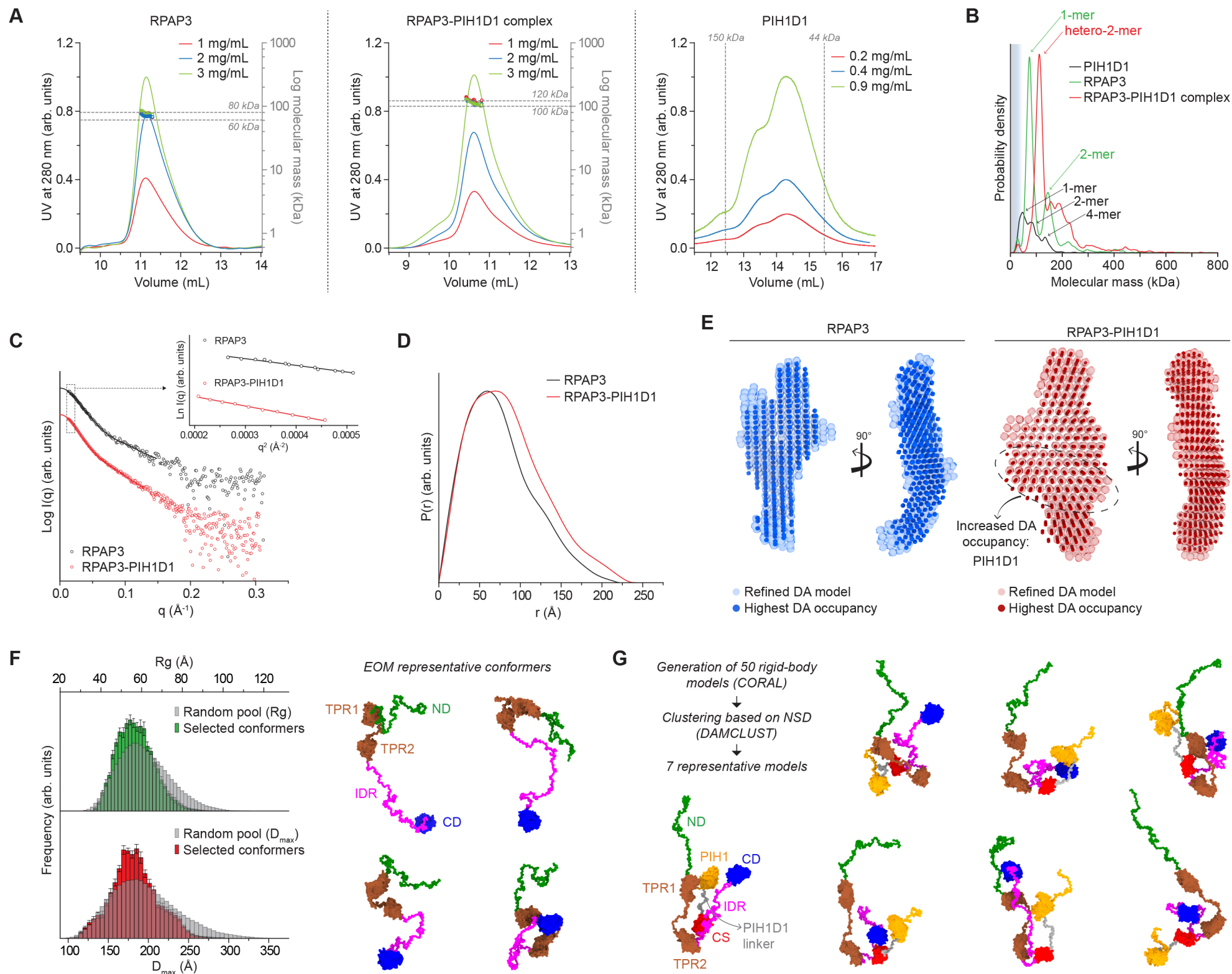


Figure 3

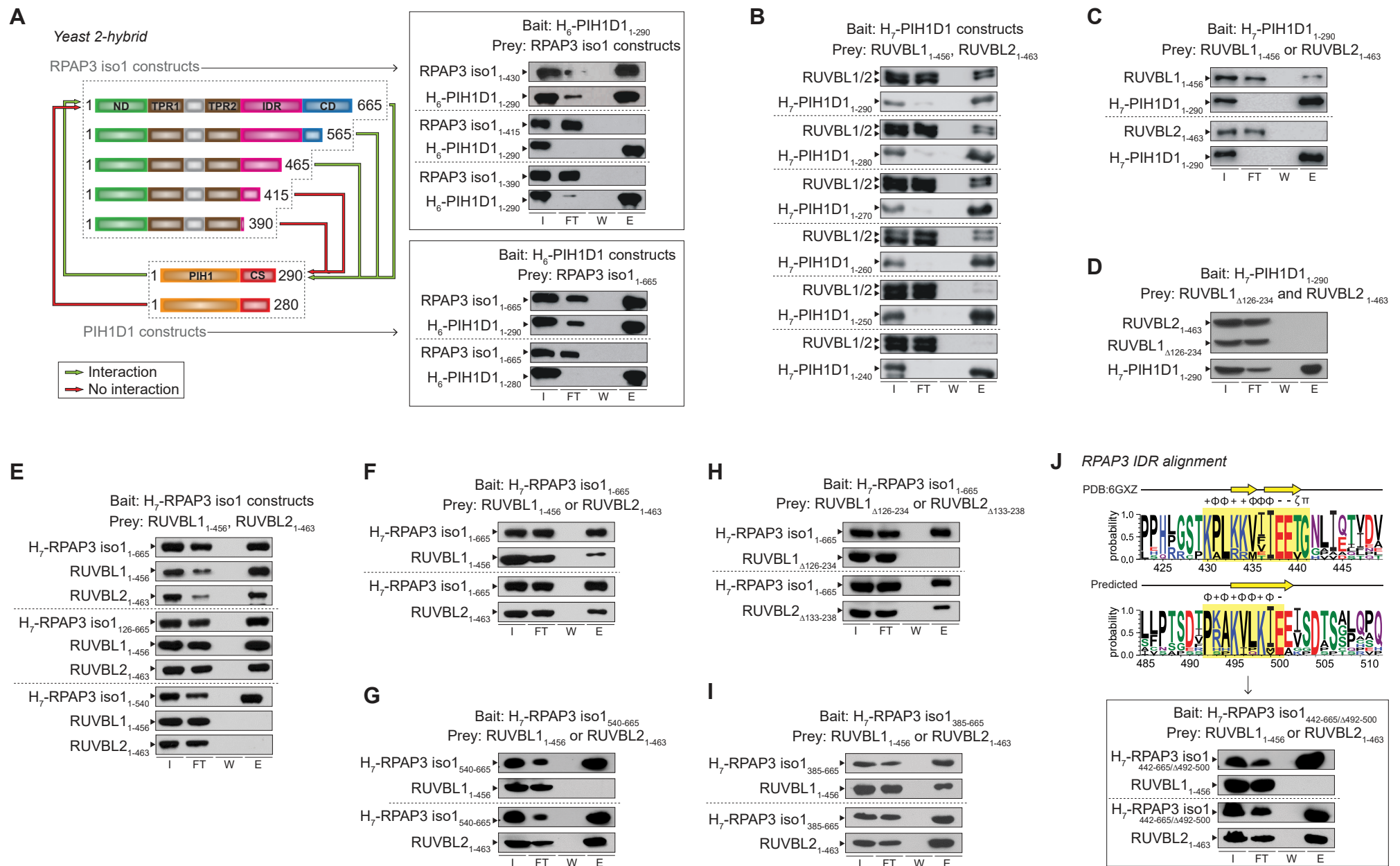


Figure 4

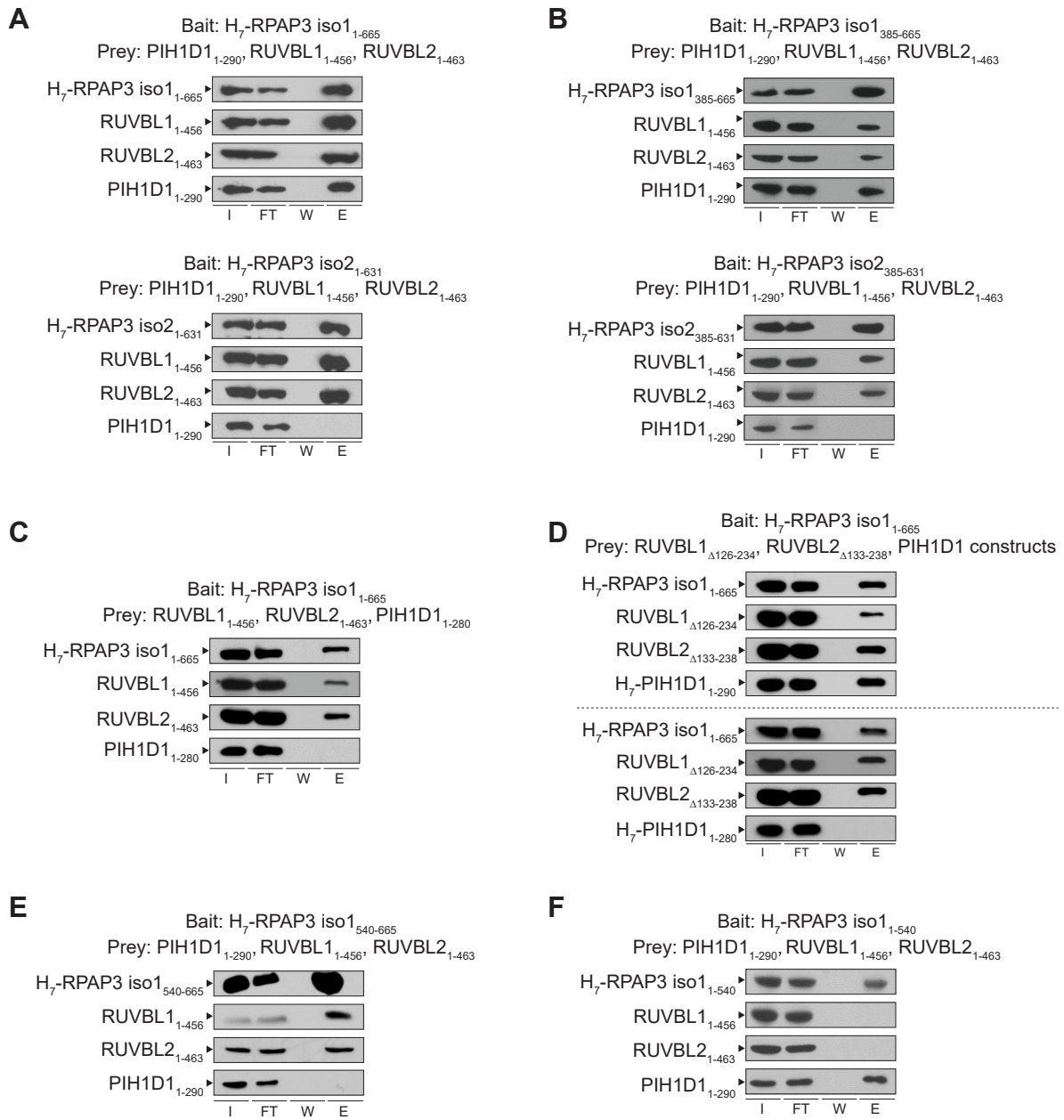


Figure 5

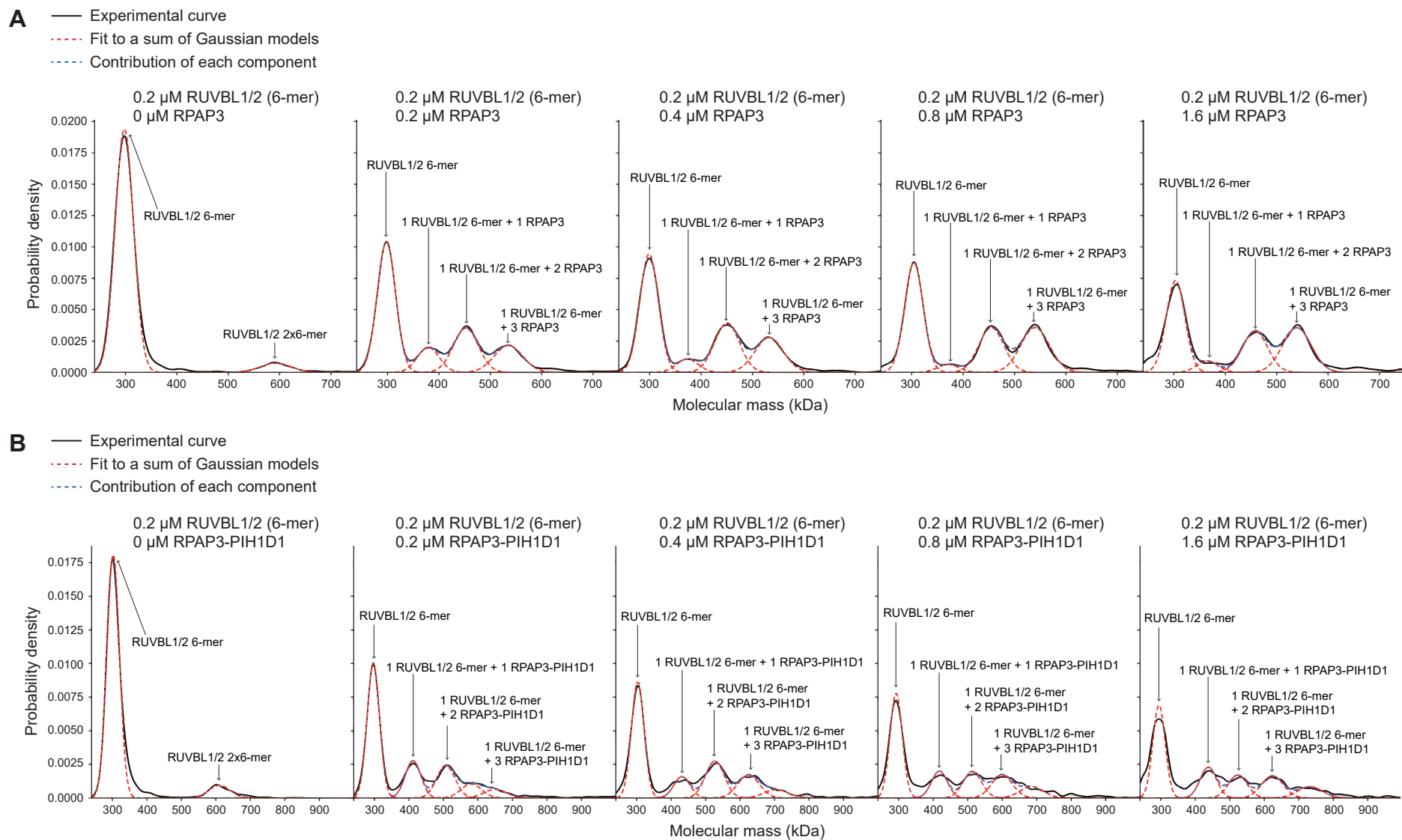


Figure 6

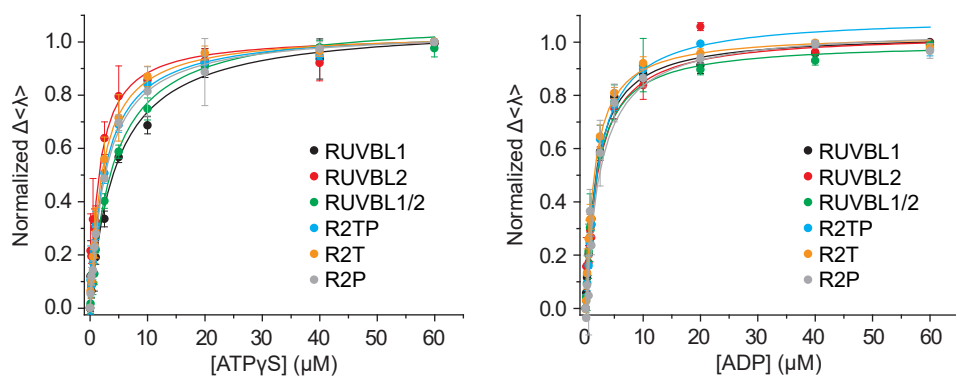
A

Kinetic parameters measured for the ATPase activity of the RUVBL proteins

Parameters	Protein		
	RUVBL1	RUVBL2	RUVBL1/2
K_M (mM)	1.29 ± 0.19	0.70 ± 0.11	0.08 ± 0.02
V_{max} (pmol Pi min ⁻¹)	31.53 ± 1.11	123.43 ± 4.64	191.02 ± 6.71
k_{cat} [pmol Pi min ⁻¹ (pmol RUVBLs) ⁻¹]	0.023 ± 0.001	0.082 ± 0.003	0.127 ± 0.004

Experiments were performed in triplicate and standard deviations are shown.

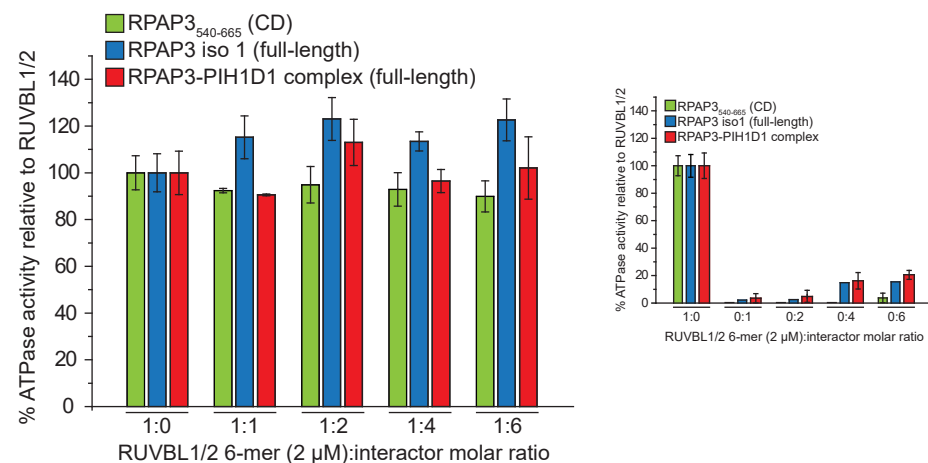
C

Apparent nucleotide dissociation constant (K_d^{app}) determined by mant-ADP experiments

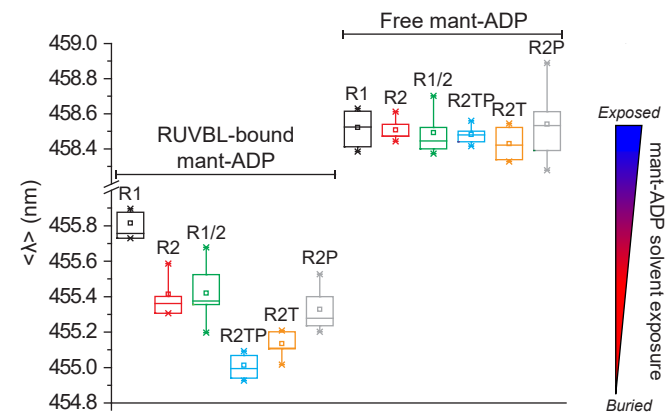
Sample	RUVBL1	RUVBL2	RUVBL1/2	R2TP	R2T	R2P
K_d^{app} (μM) ATPyS	4.5 ± 0.3	1.6 ± 0.2	4.1 ± 0.3	2.6 ± 0.2	2.2 ± 0.2	2.9 ± 0.1
ADP	1.9 ± 0.1	2.2 ± 0.2	1.9 ± 0.1	2.2 ± 0.1	1.5 ± 0.1	2.6 ± 0.3

Experiments were performed at least in triplicate and standard deviations are shown.

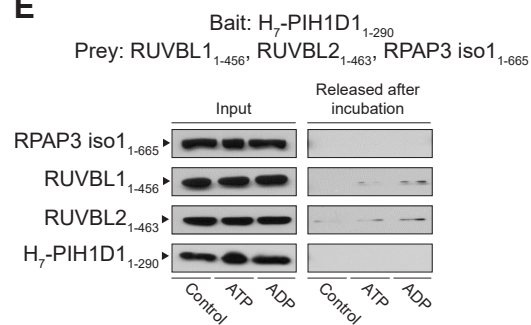
B



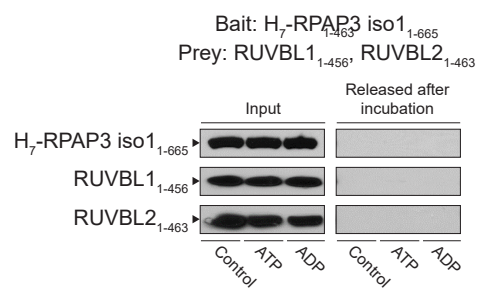
D



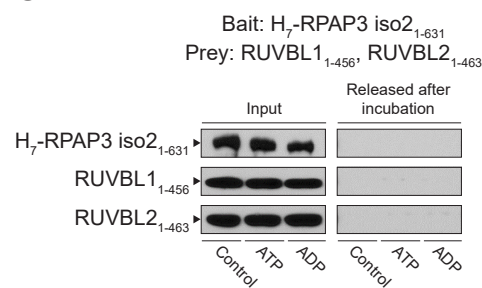
E



F



G



H

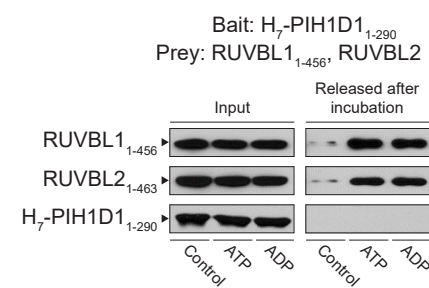
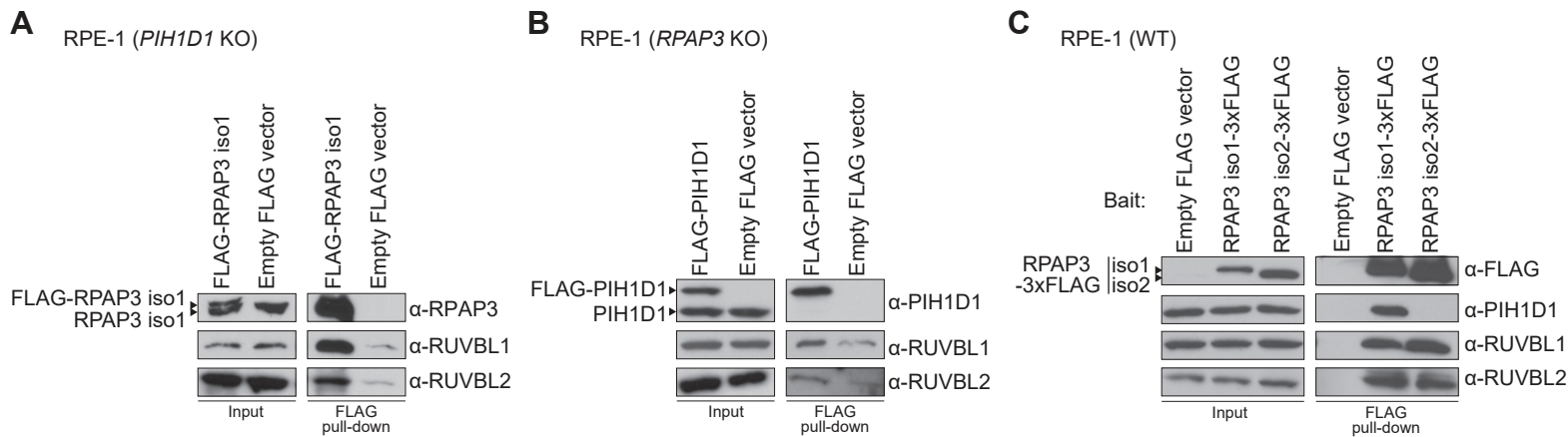


Figure 7



D RPAP3 ND-interacting proteins identified by AP-MS

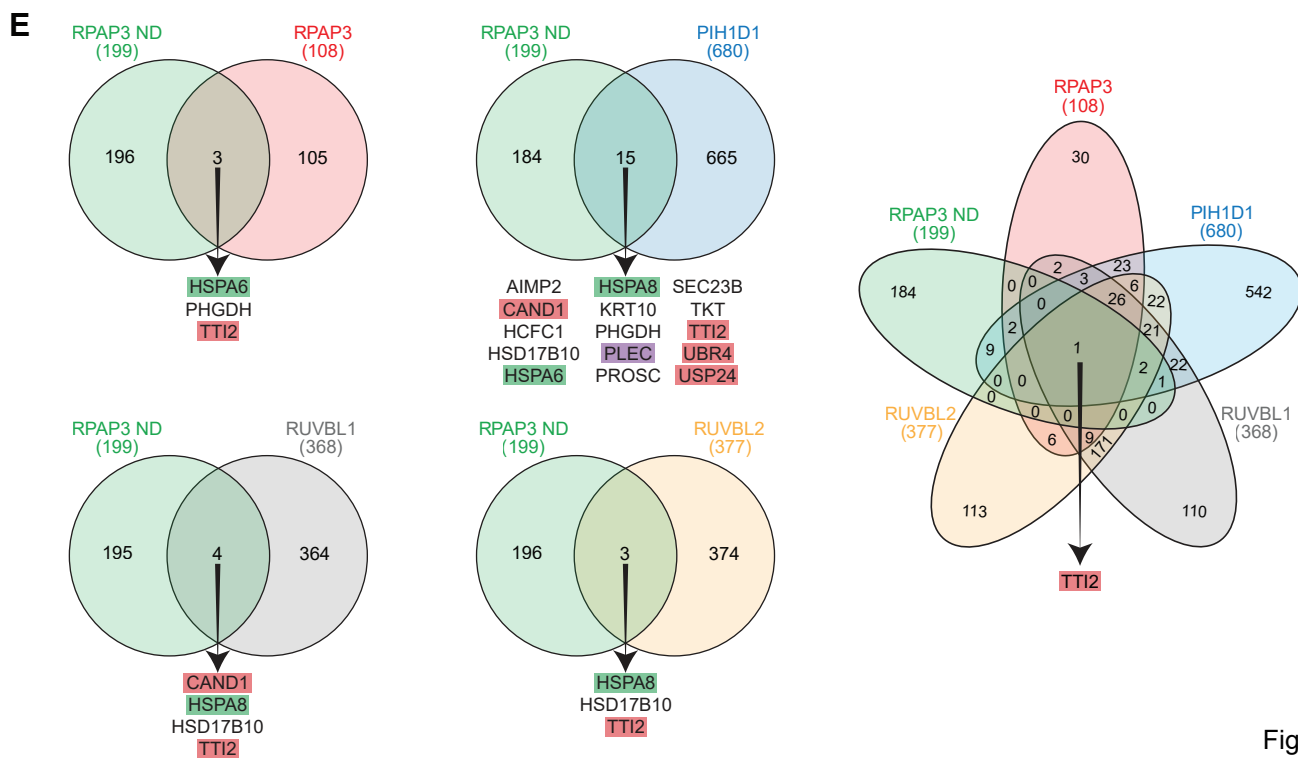
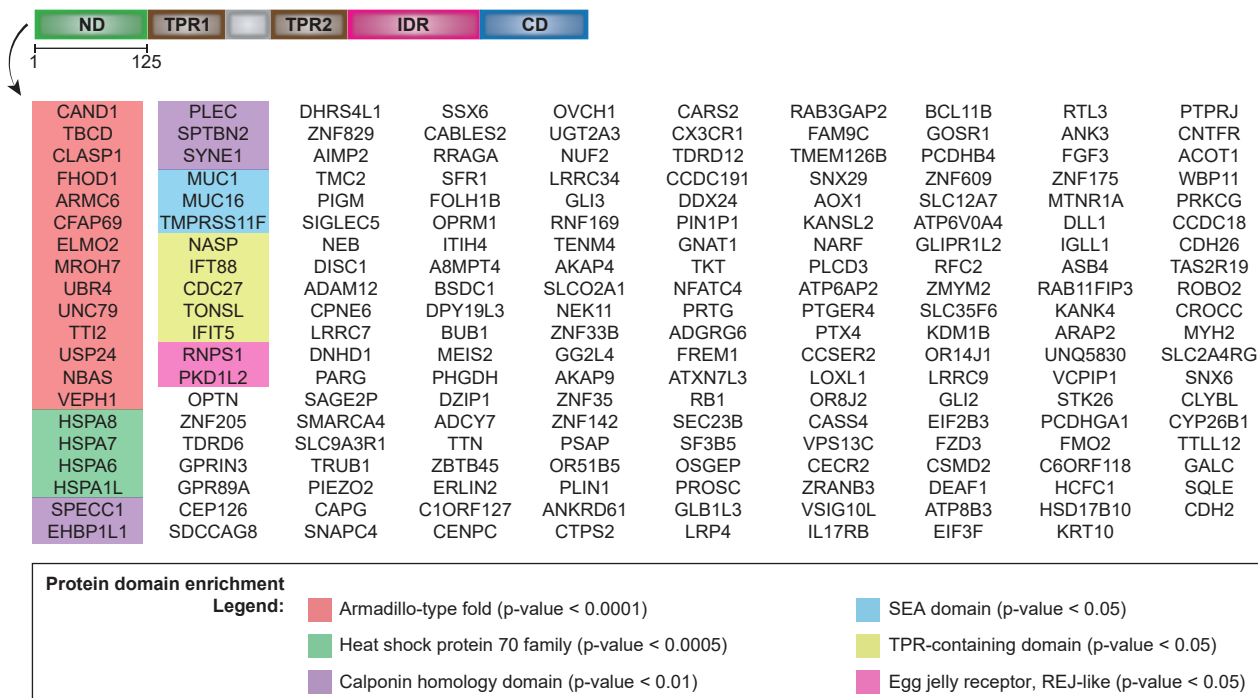


Figure 8

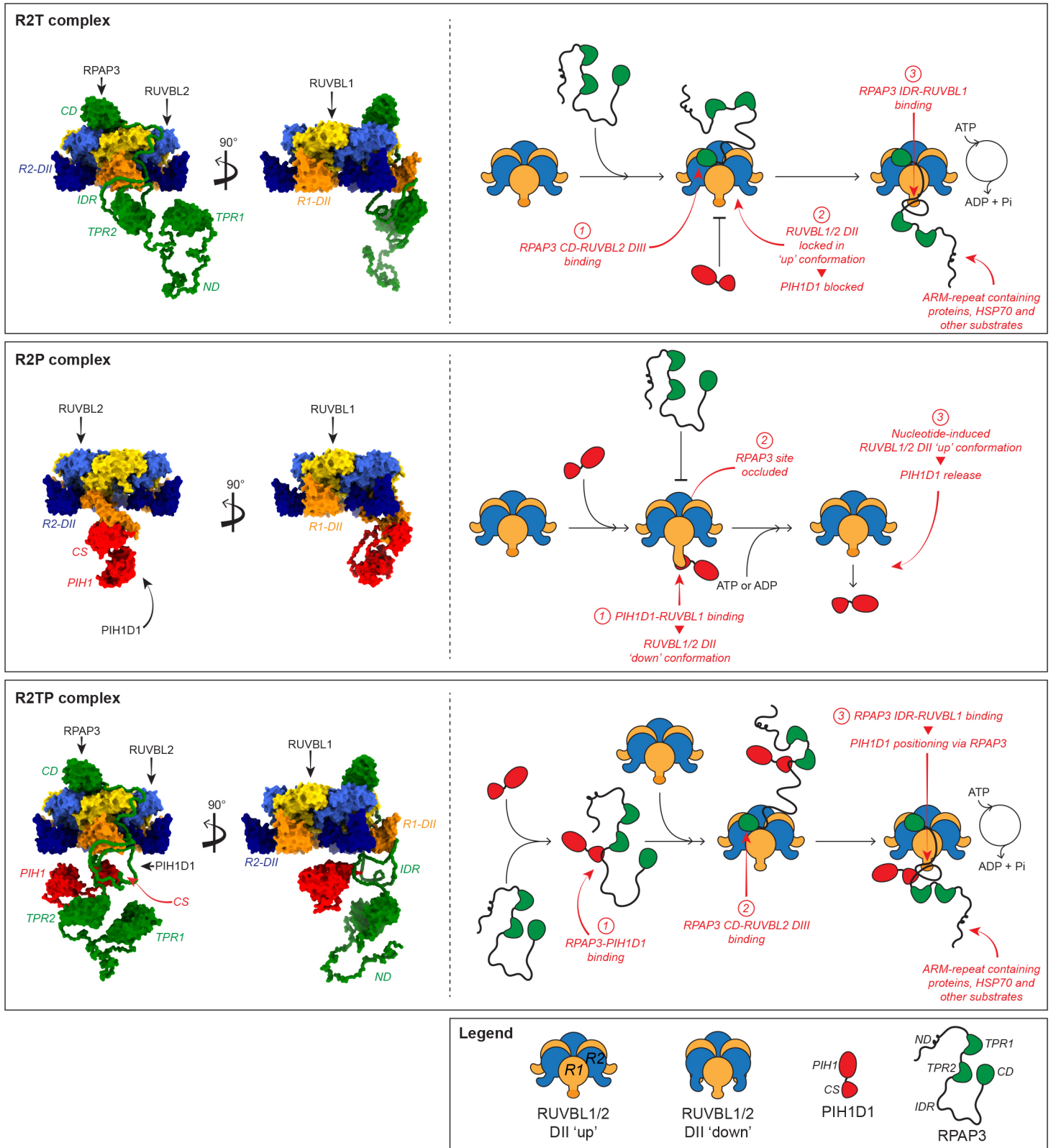


Figure 9